

11  
(2)

**AD-A233 060**

# **DIODE LASER SCALING USING UNCONVENTIONAL ADAPTIVE OPTICS**

**DTIC FILE COPY**

**W.J. Gignac, R.R. Stephens, A.A. Narayanan, R.R. Craig, and H.W. Yen**

**Hughes Research Laboratories  
3011 Malibu Canyon Road  
Malibu, California 90265**

**March 1991**

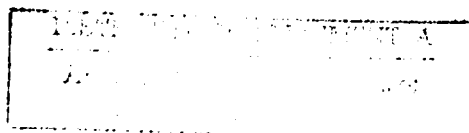
**N00014-87-C-0140**

**Final Report**

**1 April 1987 through 31 August 1990**

**DTIC  
ELECTRONIC  
MAR 27 1991  
S C D**

**OFFICE OF NAVAL RESEARCH  
800 N. Quincy Street  
Arlington, VA 22217-5000**



51 2 20 082

<b>REPORT DOCUMENTATION PAGE</b>				<i>Form Approved OMB No. 0704-0188</i>	
1a. REPORT SECURITY CLASSIFICATION <b>Unclassified</b>			1b. RESTRICTIVE MARKINGS		
2a. SECURITY CLASSIFICATION AUTHORITY			3. DISTRIBUTION / AVAILABILITY OF REPORT		
2b. DECLASSIFICATION / DOWNGRADING SCHEDULE					
4. PERFORMING ORGANIZATION REPORT NUMBER(S)			5. MONITORING ORGANIZATION REPORT NUMBER(S)		
6a. NAME OF PERFORMING ORGANIZATION <b>Hughes Research Laboratories</b>		6b. OFFICE SYMBOL <i>(If applicable)</i>	7a. NAME OF MONITORING ORGANIZATION <b>Office of Naval Research</b>		
6c. ADDRESS (City, State, and ZIP Code) <b>3011 Malibu Canyon Road Malibu, CA 90265</b>			7b. ADDRESS (City, State, and ZIP Code) <b>800 North Quincy Street Arlington, Virginia 22217-5000</b>		
8a. NAME OF FUNDING / SPONSORING ORGANIZATION <b>DARPA</b>		8b. OFFICE SYMBOL <i>(If applicable)</i>	9. PROCUREMENT INSTRUMENT IDENTIFICATION NUMBER <b>N00014-87-C-0140</b>		
8c. ADDRESS (City, State, and ZIP Code)			10. SOURCE OF FUNDING NUMBERS		
			PROGRAM ELEMENT NO.	PROJECT NO.	TASK NO.
11. TITLE (Include Security Classification) <b>DIODE LASER SCALING USING UNCONVENTIONAL ADAPTIVE OPTICS (U)</b>					
12. PERSONAL AUTHOR(S) <b>W.J. Gignac, R.R. Stephens, A.A. Narayanan, R.R. Craig, and H.W. Yen</b>					
13a. TYPE OF REPORT <b>Final</b>		13b. TIME COVERED FROM <b>4/87</b> TO <b>8/90</b>		14. DATE OF REPORT (Year, Month, Day) <b>1991 March</b>	
15. PAGE COUNT <b>70</b>					
16. SUPPLEMENTARY NOTATION					
17. COSATI CODES			18. SUBJECT TERMS (Continue on reverse if necessary and identify by block number)		
FIELD	GROUP	SUB-GROUP			
19. ABSTRACT (Continue on reverse if necessary and identify by block number)					
<p>The objectives of this program are to understand and develop technologies necessary for optimizing large area diode amplifiers that can be used in a phase conjugate (PC) master oscillator power amplifier (MOPA) arrangement to produce high power laser output.</p> <p>This report describes the study results on amplifier design, anti-reflection coating development, amplifier fabrication, and amplifier characterization.</p>					
20. DISTRIBUTION / AVAILABILITY OF ABSTRACT <input type="checkbox"/> UNCLASSIFIED / UNLIMITED <input checked="" type="checkbox"/> SAME AS RPT. <input type="checkbox"/> DTIC USERS				21. ABSTRACT SECURITY CLASSIFICATION <b>Unclassified</b>	
22a. NAME OF RESPONSIBLE INDIVIDUAL <b>Dr. Vern Smiley</b>				22b. TELEPHONE (Include Area Code) <b>619-553-6121</b>	
				22c. OFFICE SYMBOL <b>1112SL</b>	

## PREFACE

The authors gratefully acknowledge the creative and innovative technical support of D.L. Persechini, S.L. Bourgholtzer, and S.C. Ontiveros. The scientific advice and technical direction of R.C. Lind and C.R. Giuliano are also greatly appreciated.

W.J. Gignac and R.R. Craig are now at Spectra Diode Laboratories, Inc. in San Jose, CA.

A-1	
R-1	
R-2	
R-3	
R-4	
R-5	
R-6	
R-7	
R-8	
R-9	
R-10	
R-11	
R-12	
R-13	
R-14	
R-15	
R-16	
R-17	
R-18	
R-19	
R-20	
R-21	
R-22	
R-23	
R-24	
R-25	
R-26	
R-27	
R-28	
R-29	
R-30	
R-31	
R-32	
R-33	
R-34	
R-35	
R-36	
R-37	
R-38	
R-39	
R-40	
R-41	
R-42	
R-43	
R-44	
R-45	
R-46	
R-47	
R-48	
R-49	
R-50	
R-51	
R-52	
R-53	
R-54	
R-55	
R-56	
R-57	
R-58	
R-59	
R-60	
R-61	
R-62	
R-63	
R-64	
R-65	
R-66	
R-67	
R-68	
R-69	
R-70	
R-71	
R-72	
R-73	
R-74	
R-75	
R-76	
R-77	
R-78	
R-79	
R-80	
R-81	
R-82	
R-83	
R-84	
R-85	
R-86	
R-87	
R-88	
R-89	
R-90	
R-91	
R-92	
R-93	
R-94	
R-95	
R-96	
R-97	
R-98	
R-99	
R-100	

# TABLE OF CONTENTS

SECTION		PAGE
1	INTRODUCTION AND SUMMARY.....	1
	1.1 Background .....	1
	1.2 Program Objectives.....	1
	1.3 Summary .....	3
2	AMPLIFIER DESIGN CONSIDERATIONS .....	5
	2.1 Epitaxial Design.....	5
	2.2 Amplifier Dimensions.....	7
	2.3 Amplifier Interfacing .....	9
	2.4 Amplifier Gain and Facet Reflectivity.....	9
3	AMPLIFIER FABRICATION.....	13
	3.1 GaAs/GaAlAs Epitaxial Material Design.....	13
	3.2 Epitaxial Material Growth .....	17
	3.3 Amplifier Processing.....	17
	3.4 Thermal Dissipation and Die Bonding .....	25
	3.5 Dielectric Coatings for High- and Anti-Reflection Facets.....	28
	3.6 Amplifier Burn-In and Testing.....	38
4	AMPLIFIER CHARACTERIZATION.....	42
	4.1 Two-Pass MOPA Characteristics .....	42
	4.2 Amplifier Parameter Evaluation from MOPA Measurements.....	47
	4.3 Determination of $I_{SAT}$ from Laser P-I Curves .....	59
	4.4 Summary of Amplifier Parameters .....	61
	REFERENCES.....	64

## LIST OF FIGURES

FIGURE		PAGE
1	Diode Module Concept using a Single Large-Area Diode Amplifier .....	2
2	Candidate Amplifier Structures .....	6
3	Large Area Amplifier Array .....	8
4	Four-Pass PC MOPA.....	10
5	Maximum Possible Extractable Double Pass Gain from a Diode Optical Amplifier as a Function of Input Facet Reflectivity .....	12
6	GaAs/GaAlAs SWQ GRIN-SCH optical amplifier expitaxial structure .....	14
7	GaAsSQW energy as a function of well thickness .....	16
8	Photograph of the vertical bell jar MOVPE system.....	18
9	Schematic diagram of a load lock system.....	19
10	MO source gas line.....	20
11	AsH <sub>3</sub> purifier system. ....	21
12	Schematic gas flow diagram of the MOVPE system .....	22
13	P-I characteristics for a single uncoated diode laser operating CW at 14°C.....	23
14	Multi-element diode optical amplifier array.....	24
15	GaAs/GaAlAs diode optical amplifier processing sequence.....	26
16	Output power ratio for the uncoated and HR coated facets of a cleaved facet GaAs/GaAlAs diode laser as a function of the HR facet reflectivity .....	29
17	CW P-I data for diode A306-2A-A1 after one facet was coated for high reflectivity.....	30
18	Spontaneous emission spectrum from amplifier 396-2-G2 operating CW at 105 mA and 14°C .....	34
19	2-Pass MOPA technique for determining AR coated facet reflectivity ( $R_{AR}$ ).....	36
20	P-I data for diode 396-2-G2 before AR coating, and after AR coating both under high vacuum and after atmospheric exposure .....	37
21	CW P-I data for A306-2A-E5 at various stages of fabrication.....	39

## LIST OF FIGURES (Continued)

FIGURE		PAGE
22	CW P-I data for A46-D3-G10 at various stages of fabrication .....	40
23	Two-Pass, Single-End-coupled MOPA .....	43
24	Gain-Length Product Dependence on ASE and Feedback.....	44
25	Reflection-Mode Fabry-Perot Amplifier.....	46
26	Apparatus for MOPA Measurements.....	48
27	Coupling MO Beam into Amplifier.....	48
28	Facet Reflectivity and Coupling Efficiency Measurement .....	51
29	Coupling Efficiency Results .....	52
30	TE Gain-Length Product .....	54
31	TM Gain-Length Product.....	55
32	Two-Pass MOPA Output Power .....	56
33	Near-Field and Far-Field Profiles at Low Drive Currents.....	58
34	Near-Field and Far-Field Profiles at High Drive Currents .....	60
35	P-I Curves used to Determine $I_{SAT}$ .....	61

## SECTION 1

### INTRODUCTION AND SUMMARY

#### 1.1 BACKGROUND

Semiconductor diode lasers are well known for their small size, high efficiency, ease of operation, and high speed modulation capability. They are the primary source for high data rate fiber optic communication systems and compact disc players. They are also potentially important for a number of DoD systems if the output power is greatly increased. For example, high speed and high density data recording on optical discs in satellite reconnaissance systems can be made more efficient using diode lasers; inter satellite direct communication links using diode lasers can simplify the transmitter design and reduce overall weight of the spacecraft, airborne or space-based laser weapon systems using large arrays of high power diode lasers will be more efficient than other laser systems; and diode laser based blue-green submarine laser communication systems will be compact and affordable.

The output power from an injection laser is limited by a number of factors, such as the volume of the laser active region, the laser end-face damage threshold, the heat dissipation efficiency, and the desire to maintain single transverse mode operation. Several device structures have been proposed and demonstrated for achieving high power output from either a single device or an array of devices. These include: coherent coupled arrays, injection locking of arrays, self-imaging external cavity lasers, surface emitting laser arrays, etc. However, most of these approaches could not be extended to powers beyond 1 W while maintaining a nearly diffraction limited output.

The approach pursued under this contract offers a unique solution to the problem of combining the output of a large number of individual lasers or laser amplifiers. By combining the master-oscillator-power-amplifier (MOPA) approach with the nonlinear optical phenomena called phase conjugation (PC) we have shown the potential for realizing diffraction limited output well beyond the currently achievable level.

#### 1.2 PROGRAM OBJECTIVES

The objectives of this program are: (1) to understand and develop technologies appropriate to optimizing design of large area semiconductor diode amplifiers for use in a phase conjugate (PC) master oscillator power amplifier (MOPA) arrangement to produce high power laser output; (2) to fabricate and characterize large area amplifiers; and (3) to demonstrate a high power

(1 to 30 W) diffraction-limited, single frequency PC MOPA using optimized large area amplifiers.

To accomplish this goal we must study the amplifier design, develop the anti-reflection facet coating necessary to support high gain amplifiers, fabricate the amplifiers with appropriate thermal considerations, and test the PC-MOPA system to verify our design.

Figure 1 shows the basic scheme of our PC-MOPA approach. It utilizes a low power diode master oscillator and a large area power amplifier in conjunction with a phase conjugate mirror to produce an amplified, diffraction limited high power output. The amplification provided by the large area amplifier gives rise to the high output power, while any phase aberration introduced on the first pass through the amplifier are removed on the second pass by the phase conjugation process. Thus, the amplified output beam retains the highly coherent (both spatially and temporarily) properties of the low power master oscillator. This approach represents a deviation from the conventional techniques of obtaining high power from a semiconductor laser such as injection locking of lasers and using a phased array of lasers. Therefore, the limitations suffered by the conventional techniques are largely removed, allowing the use of a large area amplifier which leads to a substantially higher output power capability.

C9027-39-14

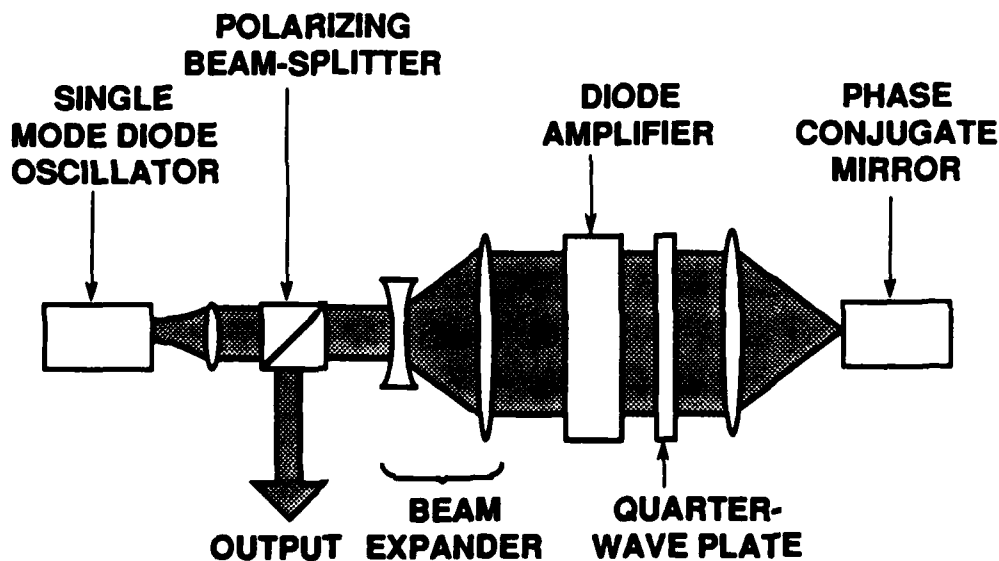


Figure 1. Diode module concept using a single large-area diode amplifier.



### 1.3 SUMMARY

This is the final report for the program, "Diode Laser Scaling Using Unconventional Adaptive Optics." Under this contract we have successfully designed, fabricated, and tested large area AlGaAs diode amplifiers appropriate for use in high power PC MOPA systems. Several amplifier structures were studied, including double heterostructure (DH), large optical cavity (LOC), and single-quantum-well, graded-index, separate confinement heterostructure (SQW GRINSCH) geometries.

We believe that the LOC version of the SQW GRINSCH structure is the best configuration for high power PC MOPA systems. This is because of its high coupling efficiency, high gain at low drive current, and high efficiency. However, good coupling efficiencies of over 40% have been measured on this contract for conventional (non-LOC) structures, so that the added complexity of incorporating the LOC into a SQW GRINSCH design may not be warranted. The majority of the data presented in this report is for amplifiers with a conventional SQW GRINSCH structure.

The major accomplishment of this program was the development of design, material growth, and fabrication capabilities for large area AlGaAs amplifiers with characteristics appropriate for use in PC MOPA systems. Growth of the basic structure is accomplished on a wafer scale by metal-organic vapor phase epitaxy (MOVPE) in a commercial system that has been extensively modified at HRL to exclude impurities and improve growth uniformity. Amplifiers are fabricated from the wafers in a series of processing steps which are all critical to the proper functioning of the final device. Processing techniques developed and optimized on this contract include those for anti-reflection (AR) coatings, high-reflection (HR) coatings, and amplifier bonding to heatsinks.

Tests performed on the amplifiers indicate that they are compatible with current PC MOPA system designs and would perform well in a low-loss system optimized for facet coupling. Small signal gain-length products of  $(g_0 - \alpha)L = 2.5$  to  $3.0$  were measured, and large signal gains of over 22 dB were demonstrated at an output power of 110 mW from a simple two-pass MOPA. AR coated facets with reflectivities as low as  $6 \times 10^{-4}$  were produced, and HR coatings were consistently 0.95 or better. Saturation parameters for the amplifiers fell in the range of 200 to 300 kW/cm<sup>2</sup>, which is typical for AlGaAs lasers. Amplifier output beam quality after two passes of the MO degraded with increasing current, but was sufficiently good to be usable with conventional phase conjugate optical systems.

The basic technologies developed on this program for single amplifier devices were subsequently used to fabricate arrays of amplifiers under USAF contract F29601-87-C-0029, "Coherent 2-D Laser Diode Array". In the USAF program, we delivered a working PC MOPA

system to the government which employed a 2x9 array of large area diode amplifiers of the SQW GRINSCH structure.

This report contains three sections in addition to the introduction and summary. In Section 2, the relative merits of the various amplifier structures are considered, and a discussion of amplifier design considerations is presented. The amplifier fabrication sequence is described in detail in Section 3, including the epitaxial material design, material growth, amplifier processing, die bonding, dielectric coatings, and burn-in and test procedures. Section 4 discusses the optical characterization of the amplifiers including measurements of small signal gain, coupling efficiency, saturation parameter, facet reflectivity, and beam quality when operated as a MOPA system.

## SECTION 2

### AMPLIFIER DESIGN CONSIDERATIONS

It is because of our unique approach of correcting beam aberrations that we are able to use diode amplifiers with very large areas in the MOPA system to generate high output power. Such devices were traditionally considered to be impractical in high brightness laser systems and little research has been conducted on these devices. One of the goals of this program is to generate an optimum large area amplifier design. Issues that must be addressed include: amplifier geometry, optical coupling efficiency, self oscillation threshold, gain saturation level, spatial nonuniformity, power efficiency, and heat dissipation.

#### 2.1 EPITAXIAL DESIGNS

The key considerations for the amplifier design in the epitaxial direction are device power efficiency and optical coupling efficiency. The basic amplifier structure is similar to that of the laser except that the cavity Q is spoiled. Thus, the epitaxial design for efficient laser operation will also be useful for amplifiers. Four different structures were considered in our study:

##### 2.1.1 Double Heterostructure (DH)

This is the basic design that consists of a GaAs active layer with two AlGaAs cladding layers, as depicted in Figure 2(a). In the figure we plot the relative aluminum concentration in the layer thickness direction. The inverse of this plot gives the refractive index distribution showing the existence of an optical waveguide. The corresponding optical mode is also shown qualitatively.

##### 2.1.2 Large Optical Cavity (LOC)

By adding one or two waveguide layers to the basic DH structure we can expand the optical mode size and thus making it easier to achieve efficient input and output coupling. There is also an added benefit of reducing the optical power density at the facet that could reduce the risk of facet degradation. The trade-off is a slight drop in device efficiency because of the smaller overlap between the optical mode and the gain (active) region as depicted in Figure 2(b).

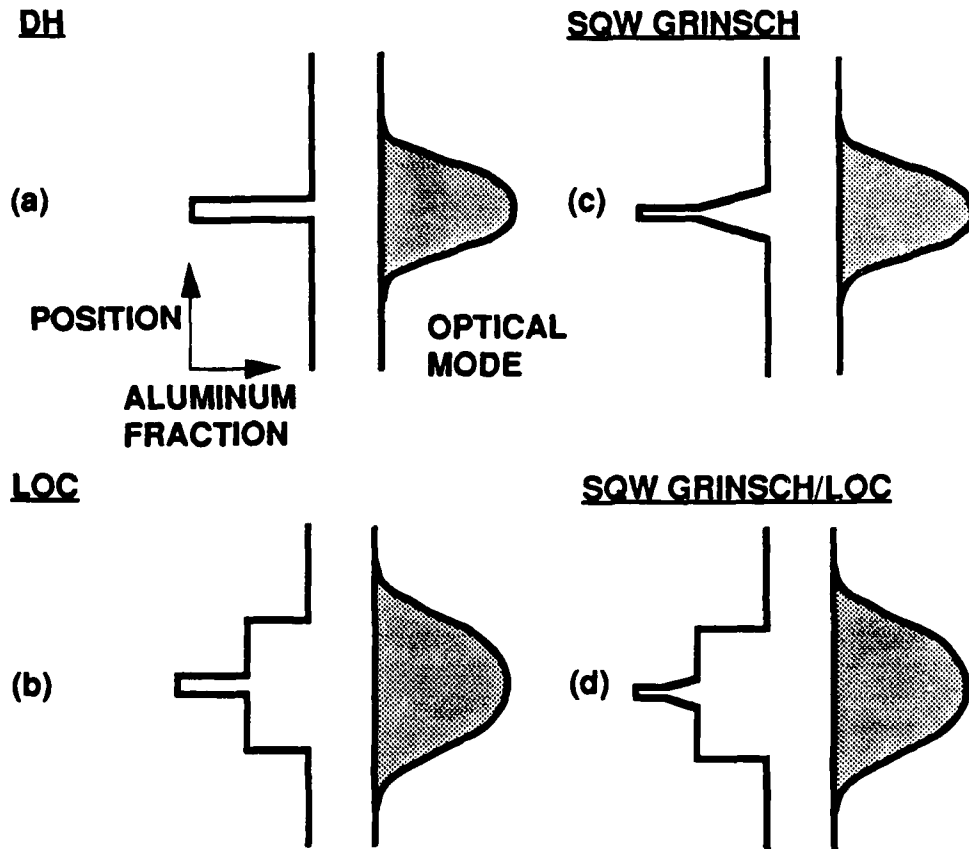


Figure 2. Candidate amplifier structures (a) double heterostructure (DH) (b) large optical cavity (LOC) (c) single quantum well (SQW) graded index separate confinement heterostructure (GRINSCH) (d) SQW GRINSCH/LOC.

### 2.1.3 Single Quantum Well Graded Index Separate Confinement Heterostructure (SQW GRINSCH)

The active region of this structure is composed of a very thin layer of GaAs (typically less than 100 Å) flanked by AlGaAs confinement layers whose aluminum concentration are graded to increase carrier confinement and recombination efficiency. The merit of using quantum confined structure for lasers or amplifiers is that high gain is reached at lower current thus leading to efficient devices. Since the mode confinement factor is smaller in this structure we expect the saturation intensity to be larger. This implies better power storage capacity when used as amplifiers. The structure is shown in Figure 2(c).

### 2.1.4 SQW GRINSCH/LOC

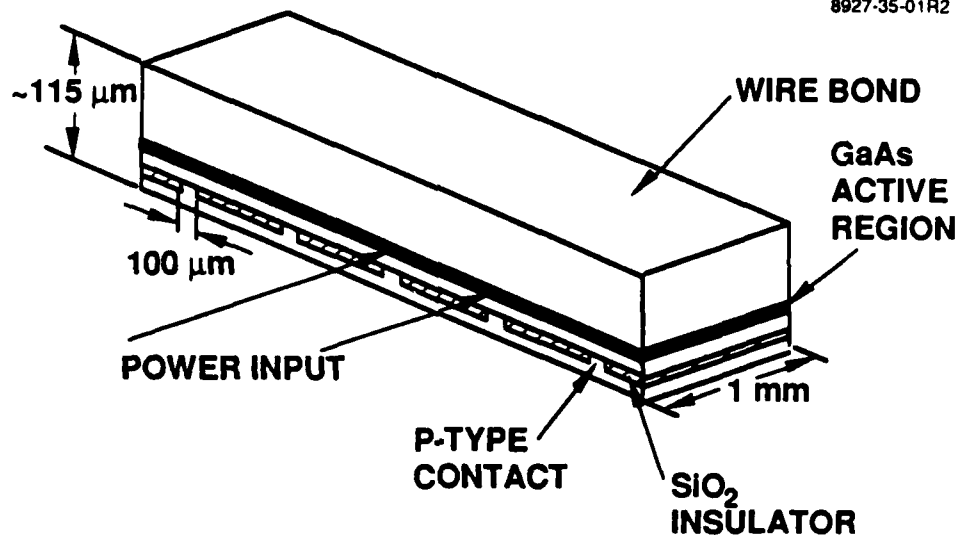
This is the large optical cavity version of the single quantum well structure. This structure is proposed because of the larger mode volume which may lead to improved coupling efficiency. A sketch of this structure is shown in Figure 2(d).

The relative merit of these structures are determined ultimately by how effectively they perform in the PC-MOPA system. But in general we can go by their effectiveness as lasers. One of the most important factor is, of course, the lasing threshold current density  $J_{th}$ . The best structure is the SQW GRINSCH because it is proven to be more efficient and less temperature sensitive compared with the conventional DH structure when operated as lasers. We believe the same advantages will carry over for amplifiers as well. Because of the small active region and finite number of energy states the QW structures reaches transparency at a lower current density and the increase in modal gain as a function of pumping current is also higher. The only issue is how to achieve a large mode size (and hence high coupling efficiency) without severely compromising the QW amplifier efficiency. Therefore, SQW GRINSCH/LOC structures with varying mode sizes must be characterized to zero in on the particular design that yields the best "system" performance.

## 2.2 AMPLIFIER DIMENSIONS

In this subsection we will discuss the amplifier length and width design issues. In a typical state-of-the-art diode laser the output power capacity is roughly proportional to the device junction area with the proportional constant of about 1 kW/cm<sup>2</sup>. Thus, if the diode is operated as an amplifier in the MOPA configuration (assuming the master oscillator produces sufficient power to saturate the amplifier) then the product of this power figure and the total junction area gives the total saturated output power of the module. For example, to obtain an output power of 100 W, the required amplifier junction area will be about 10 mm<sup>2</sup>. Assuming the maximum length (parallel to the master oscillator laser propagation direction) to be 1 mm, limited by amplified spontaneous emission (ASE), the total width of the amplifier gain region required will be about 1 cm. This large area amplifier concept is shown schematically in Figure 3. Note that the amplifier gain region is subdivided into a number of smaller sections. This is to prevent ASE in the direction transverse to the amplifier axis. Another reason to space out the amplifiers is to allow adequate heat dissipation.

In order to have efficient heat removal, i.e., operating in the condition where one dimensional heat flow model is still applicable, we must restrict the amplifier element to have a width less than 200  $\mu$ m. The estimated power loading in a large amplifier bar 1 to 2 cm wide is



- EPI-SIDE-DOWN BONDING
- 500  $\mu\text{m}$  AMPLIFIER SPACING
- $\text{SiO}_2$  PATTERNED AMPLIFIER WIDTH

Figure 3. Large area amplifier array.

on the order of 3 to 5  $\text{kW}/\text{cm}^2$ . The heat removal rate, however, is estimated to be only 0.5 to 1  $\text{kW}/\text{cm}^2$ . Therefore, to prevent the amplifier from over-heating we must introduce either temporal or spatial duty factor. Because of the desire to have cw operating capability we elect to use spatial duty factor. The amplifier width design that we select is 100  $\mu\text{m}$  and the spacing between amplifiers is 500  $\mu\text{m}$ .

In summary, the amplifier length is dictated by the desired gain-length product. Our goal for an amplifier of the type shown in Figure 3 is to achieve  $g_o L = 8$ . A longer amplifier makes it easier to reach this goal provided the amplified spontaneous emission does not render the device into oscillation first. Furthermore, because of the distributed loss along the amplifier, a long device may become less efficient. On the other hand, if the amplifier is too short, the current density required to reach the desired gain-length product may be excessive. We believe a length on the order of 1 mm is appropriate. The amplifier power capability scales with the amplifier width. But it is ultimately limited by parasitic oscillations, filamentations, and thermal considerations. We determined that a width of 100  $\mu\text{m}$  for each amplifier element is appropriate. When constructing an amplifier array, the spacing between elements should be about 500  $\mu\text{m}$  to ensure proper heat dissipation.

## 2.3 AMPLIFIER INTERFACING

The basic amplifier shown in Figure 3 requires unobstructed optical access to both front and back facets to properly function in the PC MOPA system shown in Figure 1. This is difficult to achieve considering that access space for alignment fixtures, a source of heatsink cooling, and electrical wiring must also be provided. Adopting an amplifier design that requires optical access from only one side allows the non-optical inputs to be brought in from the back as shown in Figure 4(b). This arrangement is also compatible with stacking amplifier bars vertically to form a two dimensional array. In this amplifier design the back amplifier facet is high-reflection (HR) coated and the front facet is anti-reflection (AR) coated.

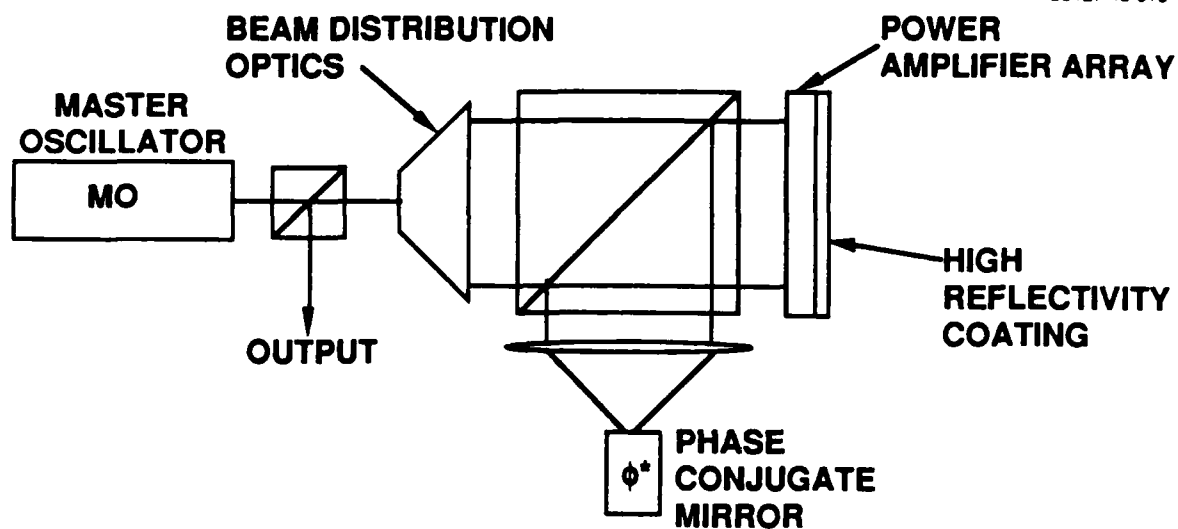
Figure 4(a) shows the four-pass PC MOPA configuration which is compatible with this approach. Light from the master oscillator (MO) couples into the amplifier through the AR coated facet, passes through the amplifier, reflects off the HR facet, and makes a second amplifier pass in the reverse direction. The amplified light then exits the amplifier and is switched into the phase conjugate mirror located in a side-arm of the system. After conjugation the light is re-coupled back into the amplifier where it again double passes the gain medium. Due to the action of the phase conjugation the phase aberrations encountered on the first set of passes are canceled after the second set, and the output of the PC MOPA will be unaberrated.

Switching beams into the phase conjugator side-arm and also coupling power out of the system is produced by polarization rotation not shown in Figure 4. The first two passes through the amplifier employ transverse electric (TE) polarization, and the second two use transverse magnetic (TM). Since light passes through the single-end coupled amplifier four times, its length can be half that of the double-end (two-pass) type shown in Figure 3 and still achieve the same overall gain. Our goal is to achieve  $g_0L = 4$  for the single-end coupled devices. Due to its relative ease of fabrication and its compatibility with external inputs, the single-end coupled (four-pass) design of Figure 4 was the sole configuration studied on this program.

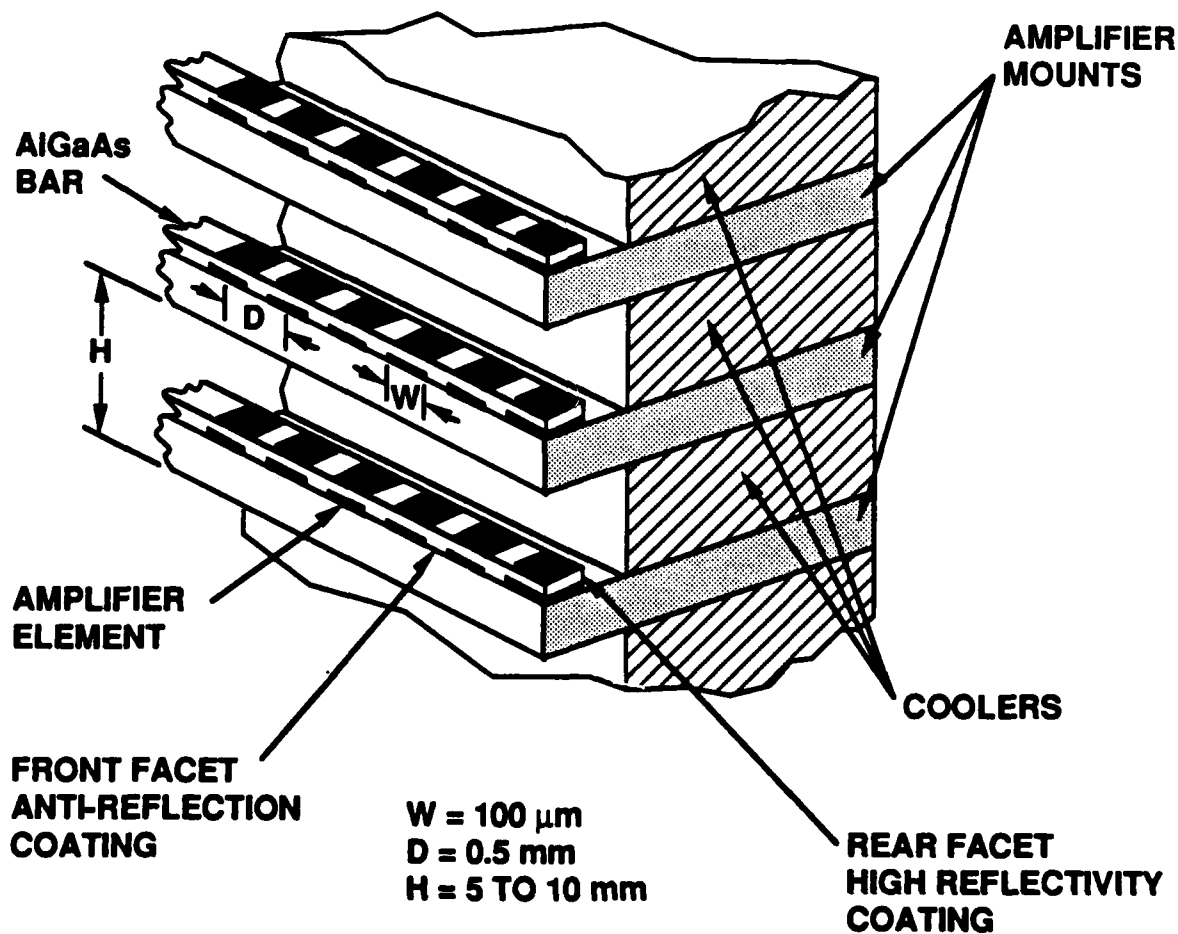
## 2.4 AMPLIFIER GAIN AND FACET REFLECTIVITY

The most significant optical factors limiting the single pass gain ( $G$ ) in an optical amplifier employing a Fabry-Perot resonator are the reflectivities of the resonator mirrors. At high enough gains and facet reflectivities, the amplifier is transformed into a laser and the gain is clamped at a fixed value. The maximum gain attainable is given by the laser threshold condition:

$$R_1 R_2 e^{2(g_0 - \alpha)L} = R_1 R_2 G^2 = 1 \quad (1)$$



(a) Basic system.



(b) Facet coupled amplifier array.

Figure 4. Four-pass PC MOPA.



where  $g_0$  is the small signal gain coefficient,  $\alpha$  the distributed loss coefficient,  $L$  the resonator length, and  $R_1$  and  $R_2$  the front and back facet reflectivities, respectively. If the resonator in our cleaved facet diode amplifier has one facet coated for high reflectivity ( $R_2=1$ ), then Eq.(1) can be rewritten to yield the following relationship between input facet reflectivity ( $R_1$ ) and the small signal gain-length product ( $g_0-\alpha$ ) $L$ :

$$(g_0 - \alpha)L = -0.5 \ln(R_1) \quad (2)$$

$G$  and  $(g_0-\alpha)L$  are maximized by minimizing facet reflectivity, and zero facet reflectivity should yield infinite gain at infinite drive current. Uncoated GaAs/GaAlAs diode facets have reflectivities of approximately 0.32, limiting  $(g_0-\alpha)L$  to 0.57. Therefore antireflection coatings are applied to the front or input facet to improve amplifier performance.

Even if zero facet reflectivities were achievable, at high optical intensities amplifier gain is limited to finite values by amplified spontaneous emission (ASE) and saturation effects. Saturation results from intrinsic restrictions on carrier injection rates in diodes, and requires the replacement of  $g_0$  by the gain coefficient ( $g$ ) in Eq. (1):

$$g = g_0 / (1 + I / I_{sat}) \quad (3)$$

where  $I$  is the optical intensity in the resonator and  $I_{sat}$  is the saturation intensity. ASE, which is present in all diodes, must be included as part of  $I$  in Eq. (3), and will limit 2-pass amplifier gain even in the absence of injected light. The commonly accepted ASE 2-pass gain limit ( $G^2$ ) for GaAs/GaAlAs diode amplifiers is 40 dB corresponding to  $(g_0-\alpha)L$  of 4.6.

In Figure 5 we show the maximum possible  $(g_0-\alpha)L$  as a function of facet reflectivity calculated from Eq. (2). Included are the ASE limit of  $(g_0-\alpha)L = 4.6$  corresponding to a reflectivity of  $1 \times 10^{-4}$ , the desired goal of  $(g_0-\alpha)L = 4.0$  with reflectivity of  $3.3 \times 10^{-4}$ , and values for a diode with one uncoated and one HR coated facet. During the course of this program several AR coating processes were investigated. The results of these studies are also shown in Figure 5, where data points for our best AR coatings and for our typical AR coatings are plotted. The best coatings produced have reflectivities of  $6 \times 10^{-4}$  and maximum gain-length products of 3.7 which is very close to our goal. More typical coatings exhibit reflectivities of  $2 \times 10^{-3}$  with corresponding maximum  $(g_0-\alpha)L$  values of 3.1. The coating processes as well as techniques for measuring AR coated facet reflectivities are described in Sections 3 and 4.

C9127-43-017

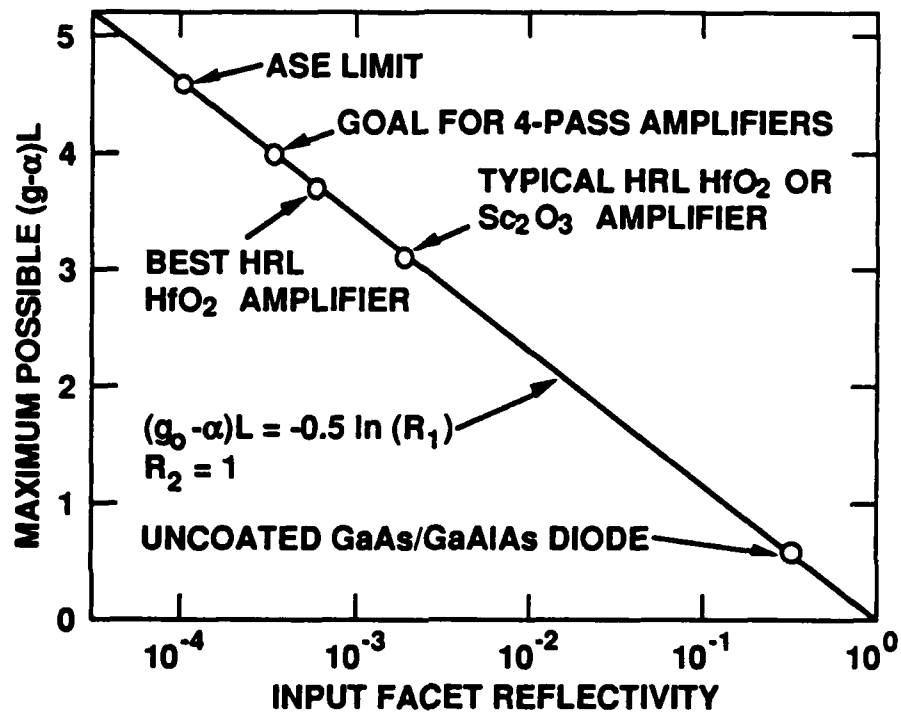


Figure 5. Maximum possible extractable double pass gain from a diode optical amplifier as a function of input facet reflectivity.

## SECTION 3

### AMPLIFIER FABRICATION

The fabrication of GaAs/GaAlAs diode optical amplifiers can be subdivided into several crucial phases: epitaxial material design, epitaxial growth, diode processing, diode to heat sink bonding, electrical lead connection, optical coating of cleaved facets, and testing. For this contract we chose a single quantum well (SQW) graded index-separate confinement heterostructure (GRIN-SCH) epitaxial design. These broad-area devices were fabricated with 100- $\mu\text{m}$ -wide by 500- $\mu\text{m}$ -long oxide defined current injection stripes. The resulting amplifiers were gain guided parallel, and index guided perpendicular, to the metallurgical junction of the diodes. One set of facets received a multilayer coating with final reflectivity in excess of 95%. The other facets were single-layer antireflection coated. Amplifiers were bonded epitaxial side down, with indium solder, to cooled copper heatsinks to ensure adequate heat dissipation. Each phase of fabrication will be discussed in detail in the following sections.

#### 3.1 GaAs/GaAlAs Epitaxial Material Design

The utility of the quantum well (QW) GRIN-SCH epitaxial design<sup>1</sup> as the basis for state-of-the-art high power GaAs/GaAlAs diode lasers has been well established.<sup>2-7</sup> Major performance advantages are two-fold: (1) low threshold current density ( $J_{th}$ ) due to high gain in the QW-GRIN regions<sup>8</sup> and good optical confinement, and (2) high external quantum efficiency ( $\eta_e$ ) arising from the high internal quantum efficiency ( $\eta_i$ ) of the QW and low optical losses in the GRIN waveguide.

For similar reasons, but with some additional constraints, the QW GRIN-SCH design should also be optimal for high power diode optical amplifiers. Amplifier performance is improved by large modal gain within the waveguide and high quantum efficiency. However, extremely tight optical confinement in QW cleaved facet devices can result in insufficient amplifier input coupling efficiency, enhanced TE over TM polarization selection<sup>9</sup> and an extremely nonplane wave optical field at the facet reducing the effectiveness of the anti-reflection coating that suppresses self-oscillation in the amplifier.<sup>10</sup> A good epitaxial design should provide optical confinement that is a compromise between high gain and the three amplifier considerations discussed above.

In Figure 6 we show a schematic representation of the GaAs/GaAlAs SQW GRIN-SCH epitaxial layer design used in amplifiers fabricated for this contract. A single rather than multiple quantum well (MQW) active region was chosen because of previous in-house experience with growth and performance of the former structure. It is possible that the MQW active region will

8927-08-231R1

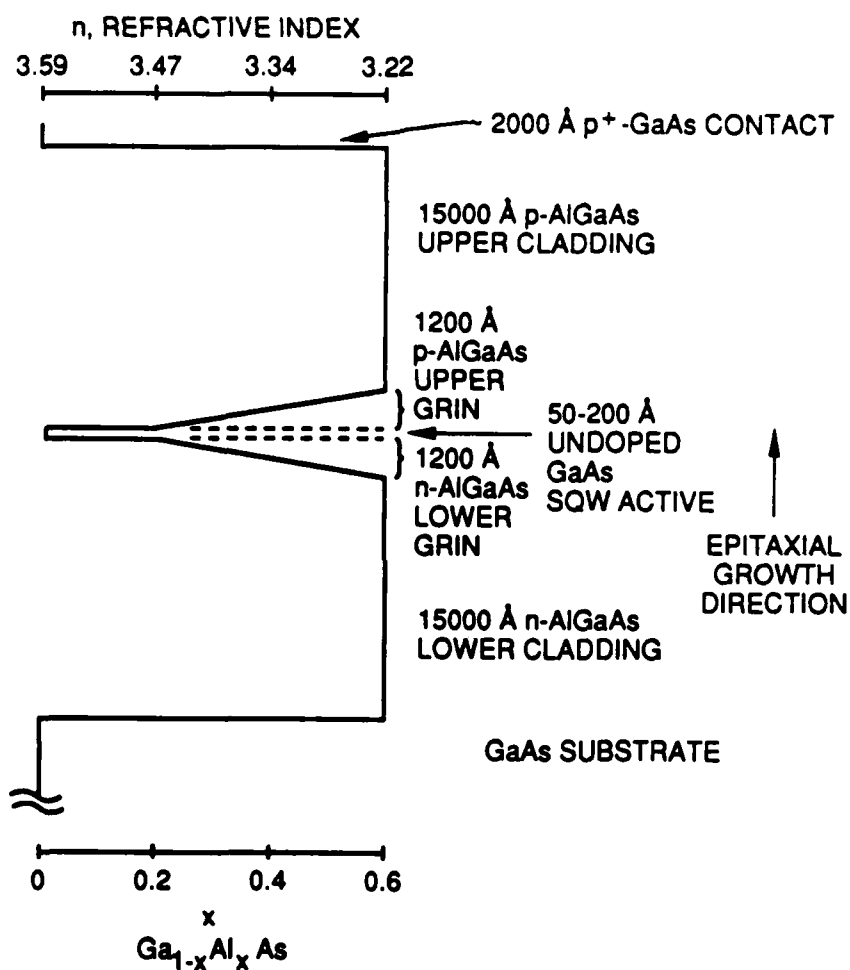


Figure 6. GaAs/GaAlAs SQW GRIN-SCH optical amplifier epitaxial structure.

provide better performance in extremely high power diode lasers because of band filling considerations, but amplifier gains are typically limited by the quality of the AR coating or thermal dissipation rather than carrier availability.

We utilized low pressure metal organic vapor phase epitaxy (MOVPE), starting with the n<sup>+</sup>-GaAs substrate (MMK, 45 mm square,  $1.3 \times 10^{18} / \text{cm}^3$  Si), to grow the diode epitaxial layers. The growth sequence was as follows. A 1- $\mu\text{m}$ -thick n<sup>+</sup>-GaAs buffer layer ( $3 \times 10^{18} / \text{cm}^3$  silicon) was grown first to correct for substrate defects. The buffer was followed by a 1.5- $\mu\text{m}$ -thick n-Ga<sub>0.4</sub>Al<sub>0.6</sub>As ( $1.2 \times 10^{17} / \text{cm}^3$  Si) lower cladding region. Then an n-type lower GRIN region was grown in which the composition was linearly graded from Ga<sub>0.4</sub>Al<sub>0.6</sub>As to Ga<sub>0.8</sub>Al<sub>0.2</sub>As. The GaAs SQW was not intentionally doped, and the width was varied to obtain the desired wavelength as discussed later in this section. The upper p-type GRIN region utilized a linear composition change from Ga<sub>0.8</sub>Al<sub>0.2</sub>As to Ga<sub>0.4</sub>Al<sub>0.6</sub>As, and was followed by the 1.5- $\mu\text{m}$ -thick p-Ga<sub>0.4</sub>Al<sub>0.6</sub>As upper cladding ( $1.2 \times 10^{17} / \text{cm}^3$  zinc). A 0.2-0.4  $\mu\text{m}$  p<sup>+</sup>-GaAs cap ( $2 \times 10^{18} / \text{cm}^3$ ) facilitated low resistivity Ohmic contact to the p-type side of the diode.

Figure 6 also shows the refractive index profile for the SQW GRIN-SCH design. The composition and thickness of GRIN regions determines the optical mode size in the epitaxial growth direction, or the direction perpendicular to the diode metallurgical junction. In all of the diode amplifiers fabricated for this project, we grew both the upper and lower GRIN regions with nominal thickness of 0.12  $\mu\text{m}$ . We also measured far-field patterns for broad area lasers fabricated from the same material as the amplifiers, and used these data to infer mode sizes ranging between 0.34 and 0.46  $\mu\text{m}$  for the various epitaxial growths.<sup>11</sup> We do not fully understand the variation in mode size from growth to growth, but feel that they are most likely due to changes in MOVPE growth parameters and conditions over the several year term of this contract. The best amplifier results were obtained with larger mode sizes, as discussed more extensively later in this section.

As stated above, the wavelength dependence of diode amplifier gain can be determined by the SQW thickness and the well and barrier compositions. For reference purposes we have included Figure 7 which shows the calculated GaAs/GaAlAs SQW conduction to heavy-hole energy as a function the SQW width. The calculation was performed at HRL by J.N. Schulman based on a two-band tight-binding model assuming a 60% GaAs valence band offset and Ga<sub>0.8</sub>Al<sub>0.2</sub>As barrier.<sup>12</sup>

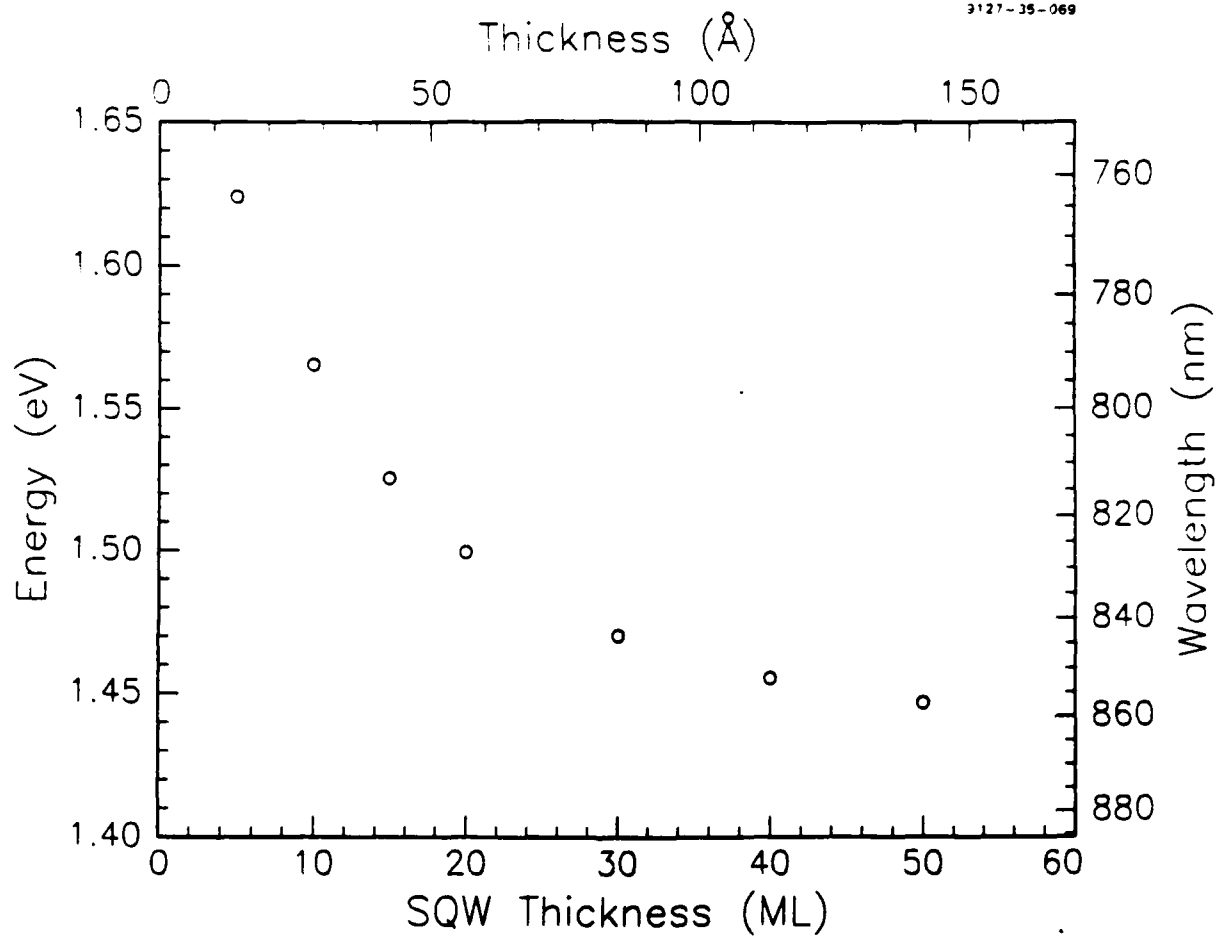


Figure 7. GaAs SQW energy as a function of well thickness. Barriers are  $\text{Ga}_{0.8}\text{Al}_{0.2}\text{As}$ .

### 3.2 EPITAXIAL MATERIAL GROWTH

The GaAs/GaAlAs epitaxial material used for amplifier fabrication was grown at HRL by metal-organic vapor phase epitaxy (MOVPE) in a system originally manufactured by Spire and extensively modified to exclude impurities and improve uniformity. Figure 8 contains a photograph of the horizontal flow, low pressure (~50 to 100 Torr) system which utilizes computerized switching of source material flow rates to achieve precise control of layer composition, thickness and doping. A turbo-molecular pump was used during a series of pump/purge cycles to ensure reactor cleanliness prior to growth. Pressure during growth was maintained by a combination of throttling valve and rotary mechanical pump. The system was also equipped with a high vacuum load lock, shown schematically in Figure 9, to facilitate the loading and removal of substrates.

The elements comprising the epi-layers (gallium, aluminum and arsenic) and dopants were introduced into the MOVPE growth chamber in the form of gaseous compounds. They were mixed together at a low temperature that precluded significant reaction, and then passed over a heated GaAs substrate wafer that served as a template for epitaxial growth. The gaseous arsenic source was AsH<sub>3</sub>, while the group III elements and dopants were introduced as organometallic alkyl compounds. The organometallic sources are liquids near room temperature, and were transported as vapors; hydrogen was bubbled through temperature regulated source containers. A schematic representation of the organometallic source gas line appears in Figure 10. Commercially obtained AsH<sub>3</sub> was purified *in situ* by passing through a heated molecular sieve trap, 0.02- $\mu$ m particle filter, GaInAl melt, and another 0.02  $\mu$ m particle filter as shown in Figure 11. The overall gas flow schematic diagram is shown in Figure 12

The system typically produces unintentionally doped GaAs layers on GaAs (100) substrates with n-type carrier concentrations in the  $10^{15}/\text{cm}^3$  range and room temperature Hall mobilities near  $6000 \text{ cm}^2\text{V}^{-1}\text{s}^{-1}$ . We have demonstrated threshold current densities of  $240 \text{ A}/\text{cm}^2$ , uncorrected for carrier diffusion, and external differential quantum efficiencies of 0.71 photons/electron for broad area, oxide defined stripe lasers with uncoated facets operating under pulsed and continuous wave (CW) conditions at 14°C. Figure 13 shows typical optical power versus injected current (P-I) data for an uncoated diode laser operated CW at 14°C.

### 3.3 AMPLIFIER PROCESSING

The amplifiers fabricated on this contract are 100  $\mu$ m wide and 500  $\mu$ m long. The gain region is limited to the 100  $\mu$ m dimension by oxide defined current injection stripes. A large number of gain regions are defined side-by-side on the AlGaAs wafer with center-to-center element

MC18173

16102-12R1



Figure 8. Photograph of the vertical bell jar MOVPE system.



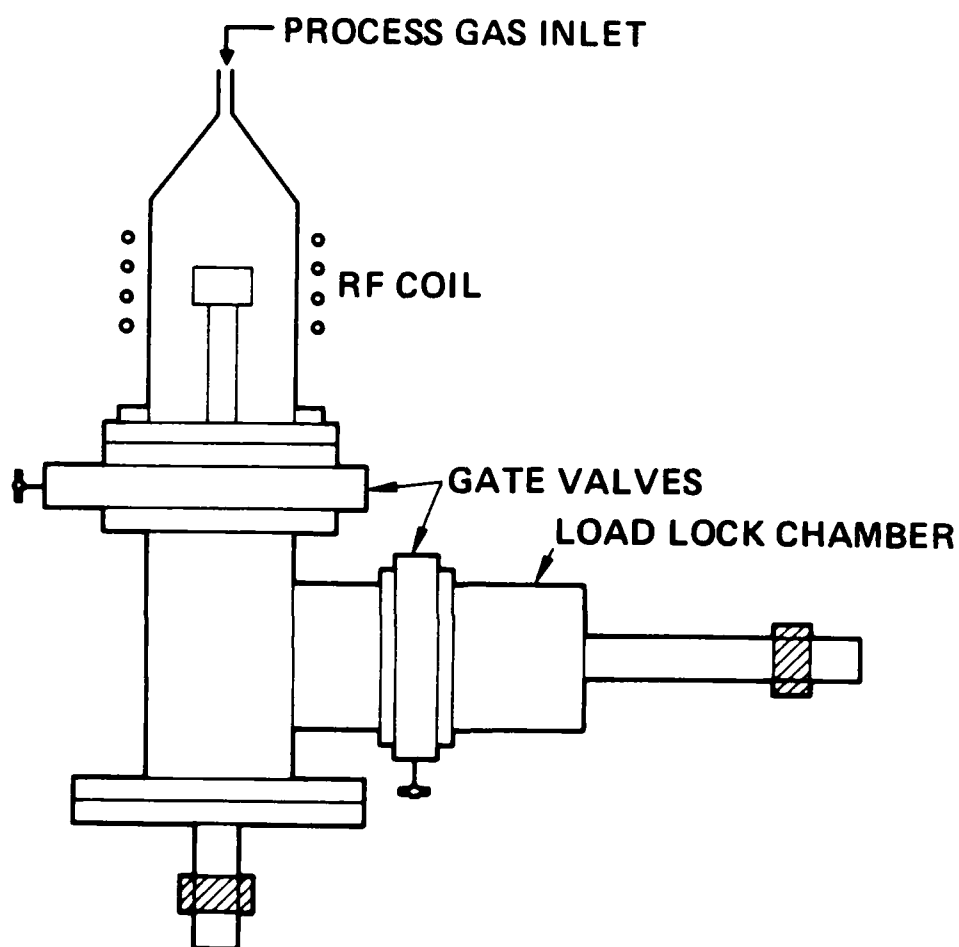


Figure 9. Schematic diagram of a load lock system.

14943-8

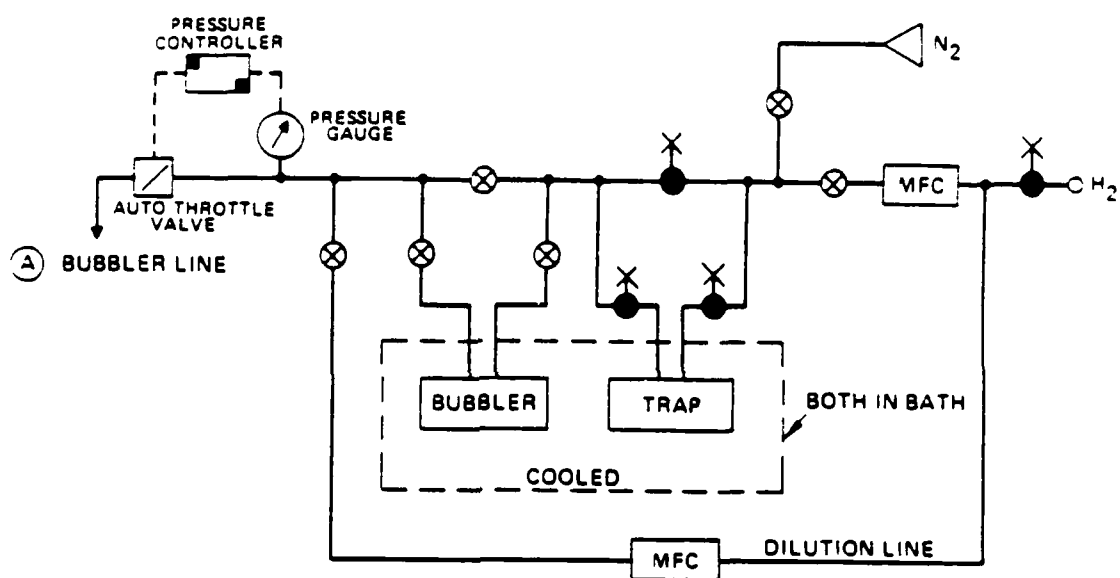


Figure 10. MO source gas line.

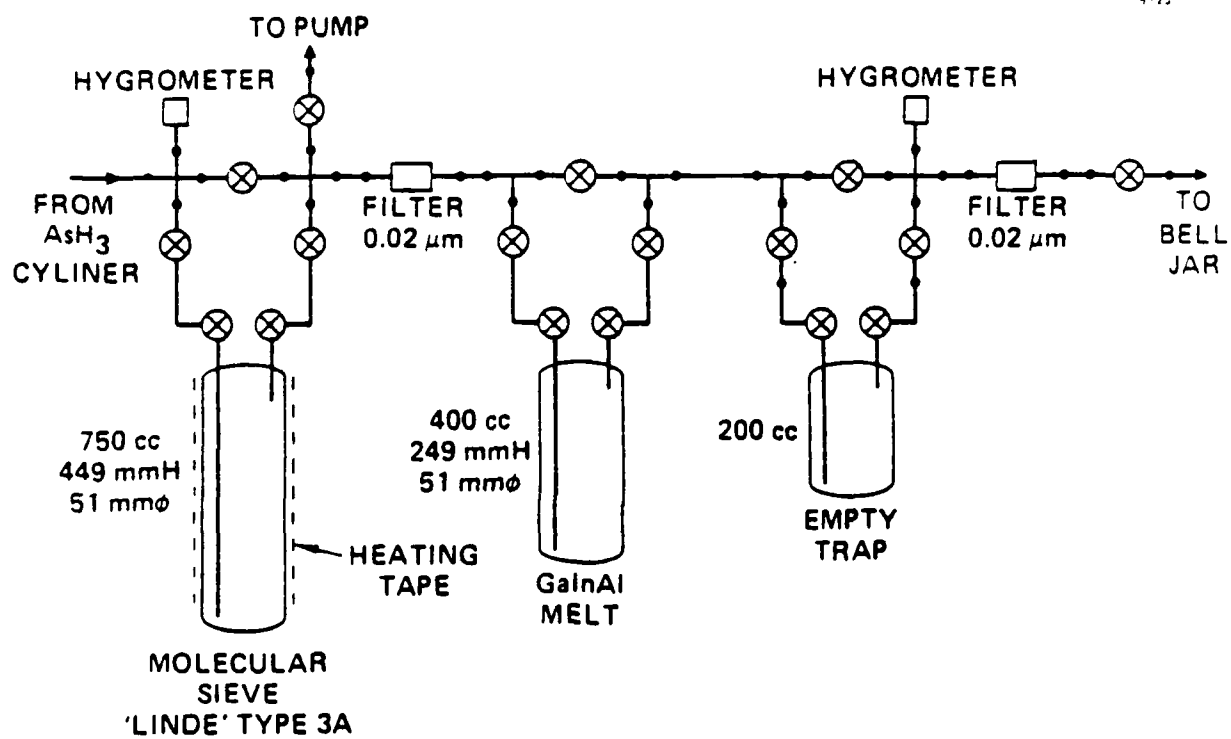


Figure 11.  $\text{AsH}_3$  purifier system.

14943-9

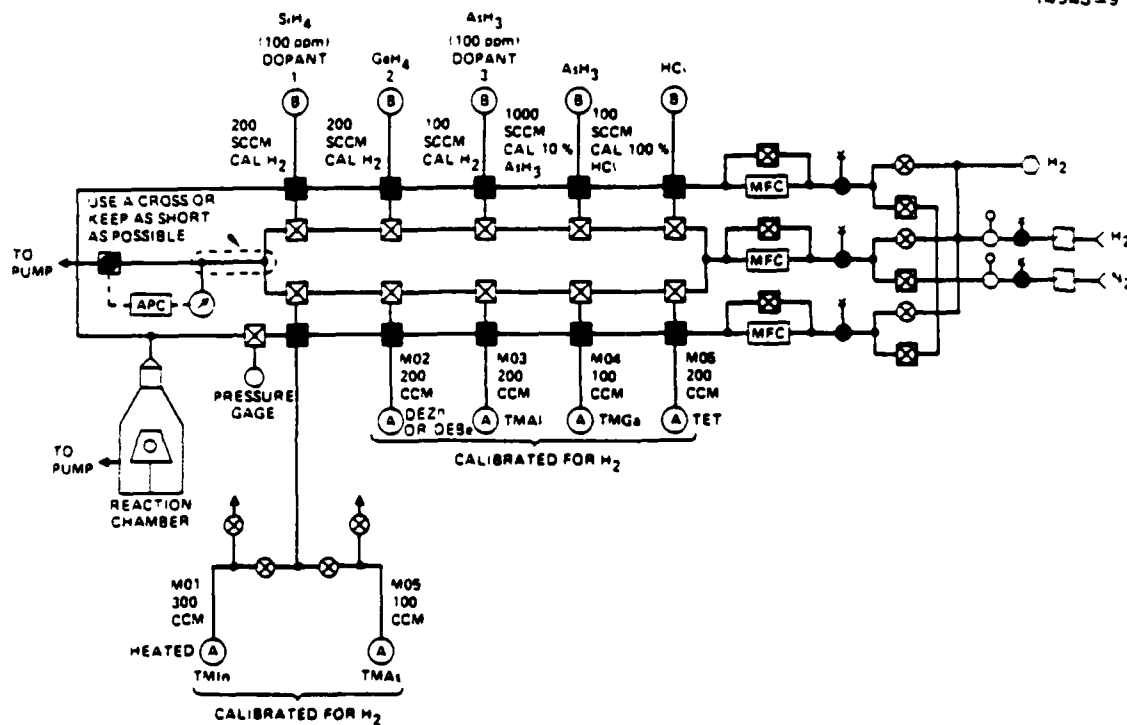


Figure 12. Schematic gas flow diagram of the MOVPE system.

9127-35-070

A306-2A-B1, 14 °C, Uncoated Facets

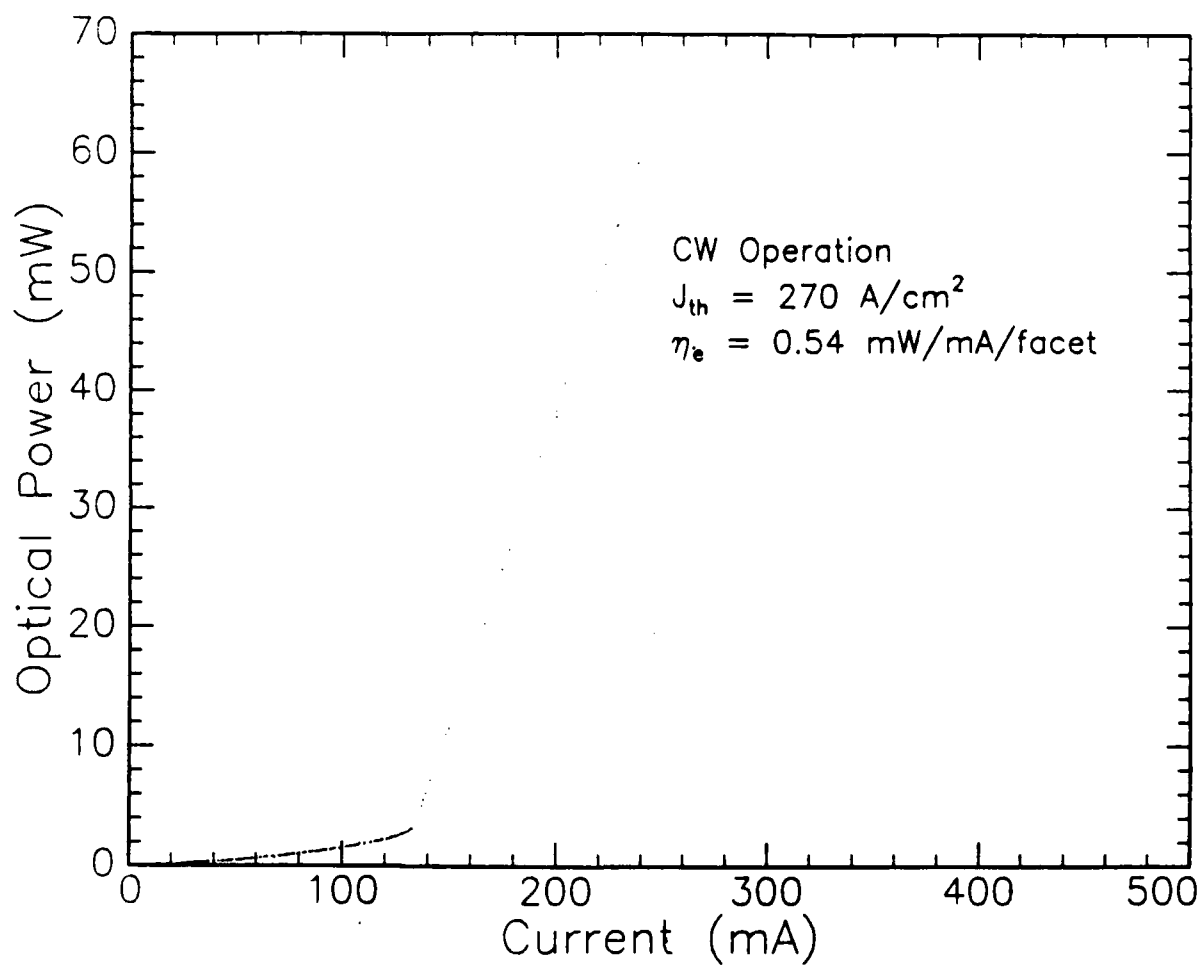


Figure 13. P-I characteristics for a single uncoated diode laser operating CW at 14°C.

spacings of 500  $\mu\text{m}$ . After processing, single amplifiers are created by dicing individual elements from the fabrication bars. The amplifiers may also be left in bar form to facilitate electrical, optical, and uniformity testing. Test bars typically had eleven gain elements; part of a bar of amplifiers is shown schematically in Figure 14.

8927-C8-230R1

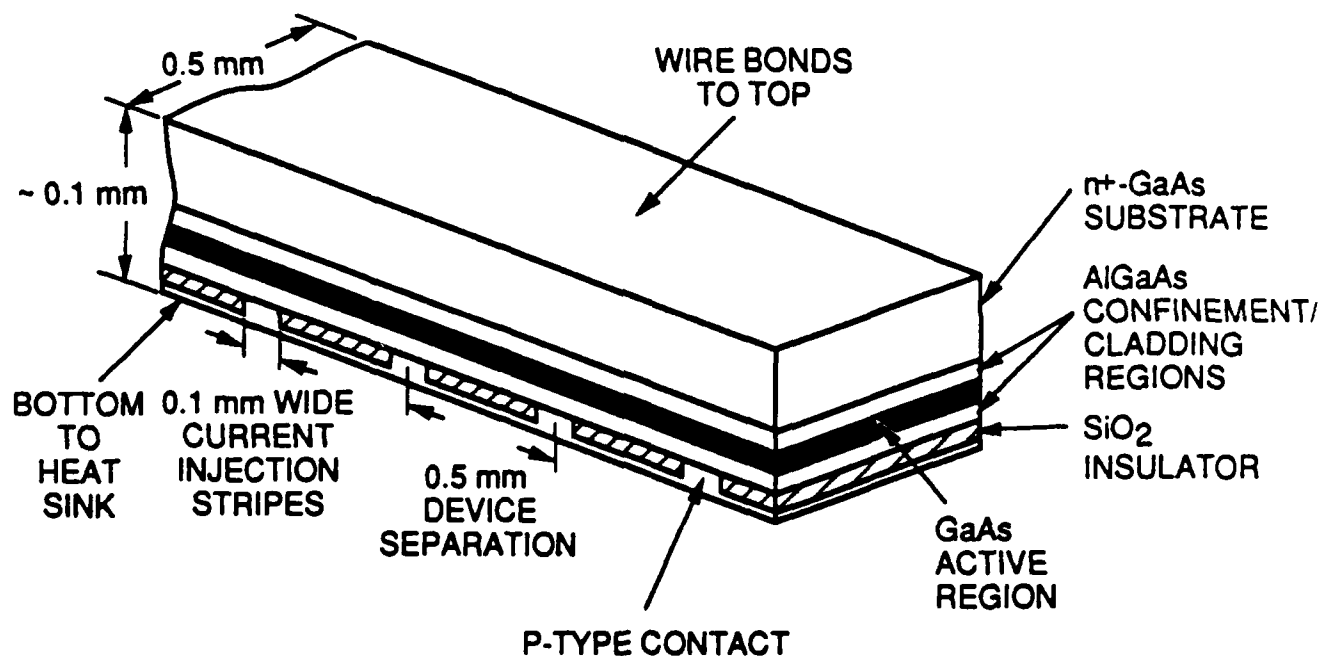


Figure 14. Multi-element diode optical amplifier bar.

The diode optical amplifier processing sequence is depicted diagrammatically in Figure 15. Between 1000 and 2000 Å of SiO<sub>2</sub> was sputtered onto the MOVPE grown p<sup>+</sup>-GaAs cap layer. Photoresist was applied to the SiO<sub>2</sub> and patterned into 100-μm-wide stripes. Commercial buffered oxide etch (BOE) was used to etch 100-μm stripes through the SiO<sub>2</sub>. The wafer then received a quick series of surface oxide removal etches: NH<sub>4</sub>OH:H<sub>2</sub>O (1:15), HCl:H<sub>2</sub>O (1:15) and again NH<sub>4</sub>OH:H<sub>2</sub>O (1:15), and was immediately loaded into an electron-beam (E-beam) evaporator for a blanket 340 Å manganese followed by 2000 Å of gold. The photoresist and metal were then removed from the SiO<sub>2</sub> by a lift-off process, leaving 100 μm wide Mn/Au stripes on the p<sup>+</sup>-GaAs cap in between 400-μm stripes of SiO<sub>2</sub>. An Ohmic contact to the p-type GaAs was obtained by sintering at 420°C for 60 s in a rapid thermal annealer (RTA).

The wafer was then thinned from the n<sup>+</sup>-GaAs substrate side to ~100 μm. Thinning enabled high quality facets to be formed by cleaving later in the process. Immediately after another series of surface oxide etches, a blanket metallization consisting of successive E-beam evaporated layers of 1000 Å Au:Ge, 400 Å nickel and 1000 Å Au:Ge was applied to the n<sup>+</sup>-substrate. The n-type Ohmic contact was finished by sintering for 60 s at 400°C in an RTA. A blanket 150 Å titanium, 2000 Å gold finished the substrate side of the wafer.

Processing on the epitaxially grown side of the wafer was finished by patterning 60 μm photoresist stripes on SiO<sub>2</sub> parallel to, and centered between, the Mn/Au p-type Ohmic contact stripes. A blanket 150 Å titanium, 1000 Å platinum and 400 Å gold metallization was followed by removal of the 60-μm photoresist stripes and overlaying metal. The resulting stripes were electrically isolated from each other, facilitating individual testing of laser diodes in bar form.

Laser bars were formed by successive cleaves at 500-μm intervals in the processed wafers, and perpendicular to the current injection stripes. Well cleaved facets result in Fabry-Perot resonators with ~32% reflectivity. Single Amplifiers are formed by dicing out individual diodes from bars.

### 3.4 THERMAL DISSIPATION AND DIE BONDING

In order to dissipate the heat generated in high power, CW diode optical amplifiers required for the PC MOPA, while maintaining low diode junction temperatures, we undertook a conservative approaches to array geometry and heat sinking. All amplifiers were bonded epitaxial-side down. This left only about 2 μm of GaAlAs between the amplifier active regions and the heat sink solder. Epitaxial-side up bonding would have placed in excess of 100 μm between active region and heat sink solder, most of it substrate GaAs.

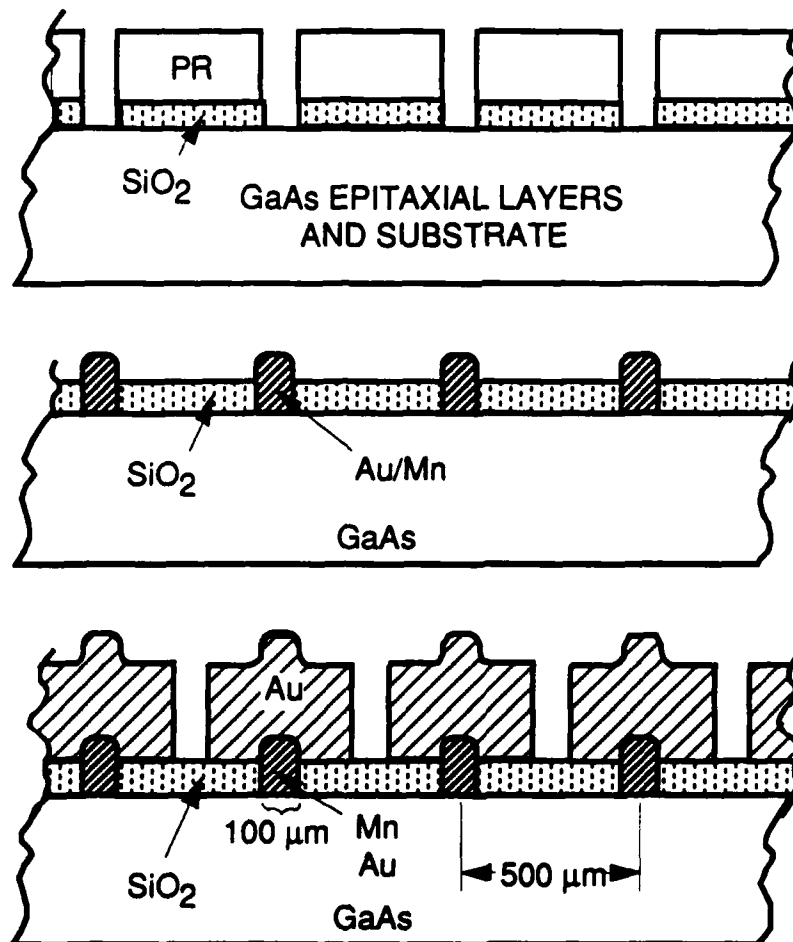


Figure 15. GaAs/GaAlAs diode optical amplifier processing sequence.



Heatsinks for single diode amplifiers were purchased from Kyocera. They were machined from a 12.5% Cu/87.5% W alloy, and finished with gold plating. Amplifier test bars were mounted on water-cooled heatsinks fabricated at HRL from oxygen-free-high-conductivity copper. These heat sinks have a water channel running only 125  $\mu\text{m}$  below the amplifier mounting surface to ensure adequate cooling of the multiple amplifiers.

If sufficient cooling capacity is available from the heatsink, then the key to heat dissipation in CW amplifiers is elimination of voids in the solder between the current injection stripes and heat sinks. Additionally, the facets must not be obstructed by solder or contaminants because light from the master oscillator must be coupled into and out of the amplifiers, and both low- and high-reflectivity coatings were applied after bonding. This requirement was especially stringent due to epi-side down bonding which places the emission aperture only  $\sim 2 \mu\text{m}$  above the heatsink. A recent study has also shown that solder flux can contaminate facets or their coatings degrading optical performance.<sup>13</sup>

To fulfill the requirements listed above we utilized a fluxless indium soldering technique.<sup>14</sup> Between 2 and 3  $\mu\text{m}$  of indium were evaporated onto specially prepared copper heatsinks. Evaporation was performed in a high vacuum system from a resistively heated source where the source to heatsink distance has been made as large as possible ( $\sim 25 \text{ cm}$ ) to minimize the temperature at the heatsinks during evaporation. High evaporation rates, 50 to 60  $\text{\AA}/\text{s}$ , were used to reduce oxygen incorporation in the indium films.

Before indium evaporation, copper, or nickel plated copper, heatsinks received the following e-beam evaporated series of metals: 200  $\text{\AA}$  of titanium, 1500  $\text{\AA}$  of nickel, 1500  $\text{\AA}$  of platinum and 400  $\text{\AA}$  of gold. The nickel and platinum layers served as diffusion barriers between copper and indium. The platinum layer in the p-type array metallization was also intended to reduce formation of Au/In intermetallic compounds.

The indium-coated heatsinks were placed on a heater stage with initial temperature less than  $35^\circ\text{C}$ . Laser/amplifier dice were placed p-side down on the heatsinks, and manipulated and held in place with micropositioners. The region surrounding the dice and heat sinks were purged for 5 m with forming gas (10%  $\text{H}_2$  in  $\text{N}_2$ ), and the heater temperature was raised to  $165^\circ\text{C}$  over a period of approximately 1.5 m, held for from 10 to 60 s, and ramped down to less than  $100^\circ\text{C}$  before the heatsink and attached diode were removed from the heater. We used the indium solder as soon as possible after evaporation, never more than 4 h, to minimize indium oxidation that is detrimental to bonding.

Electrical connection between the n-type side of the diode and external power supplies was established by wire bonding to a flying lead. We used a commercial thermo-compression wire

bonder with 32- $\mu\text{m}$ -diam Au/Be wire. There were typically two to three wires per 100x500- $\mu\text{m}^2$  diode element.

Early in the program we had problems die- and wire-bonding diodes after high-reflection dielectric coating of either facet. The diode die- and wire-bonding surfaces were contaminated with thin dielectric films that precluded adequate adhesion of indium solder or Au/Be wire. We ultimately resolved this problem by dielectric coating after both die- and wire-bonding.

### 3.5 DIELECTRIC COATINGS FOR HIGH- AND ANTI-REFLECTION FACETS

#### 3.5.1 High-Reflectivity Facets

Throughout the course of this program we used a high reflectivity coating procedure that has consistently yielded facet reflectivities greater than or equal to 95%, the limit of our standard measurement technique. The coating consisted of alternating layers of  $\text{Al}_2\text{O}_3$  and silicon to a total of six layers. Each layer thickness was chosen to be one quarter of the diode amplifier wavelength ( $\lambda/4n$  where  $\lambda$  is the diode free-space wavelength and  $n$  the refractive index of silicon or  $\text{Al}_2\text{O}_3$ ). The target thicknesses for  $\text{Al}_2\text{O}_3$  and silicon layers were 244 and 112 nm, respectively.

The dielectric coatings were fabricated by E-beam evaporation in a commercial CHA high vacuum system. The base pressure before evaporation was typically  $<1 \times 10^{-6}$  Torr. The diode temperatures varied between 20°C at the start of the depositions, and 80°C at the end, because no active cooling of the diodes was used.

The following simple equation relates the ratio of output powers from the two facets of a laser employing a Fabry-Perot cavity with the facet reflectivities,

$$I_1/I_2 = (R_2/R_1)^{1/2}(1-R_1)/(1-R_2), \quad (4)$$

where  $I_n$  are the intensities from, and  $R_n$  the reflectivities of the respective facets. We determined the reflectivity of the coated facet by measuring the intensity ratio above threshold, and assumed that the uncoated facet had a reflectivity of 32%. Figure 16 shows the intensity ratio as a function of the reflectivity of the HR coated facet assuming reflectivities of 30 and 32% for the uncoated facet. The major source of error with this technique is the inclusion of stray light during the intensity measurement from the HR coated facet. Power emitted from the uncoated facet is particularly troublesome in this regard.

Figure 17 shows the optical power as a function of injected current (P-I) for a diode laser after HR coating one facet. The intensity ratio of the power output from the uncoated to HR coated

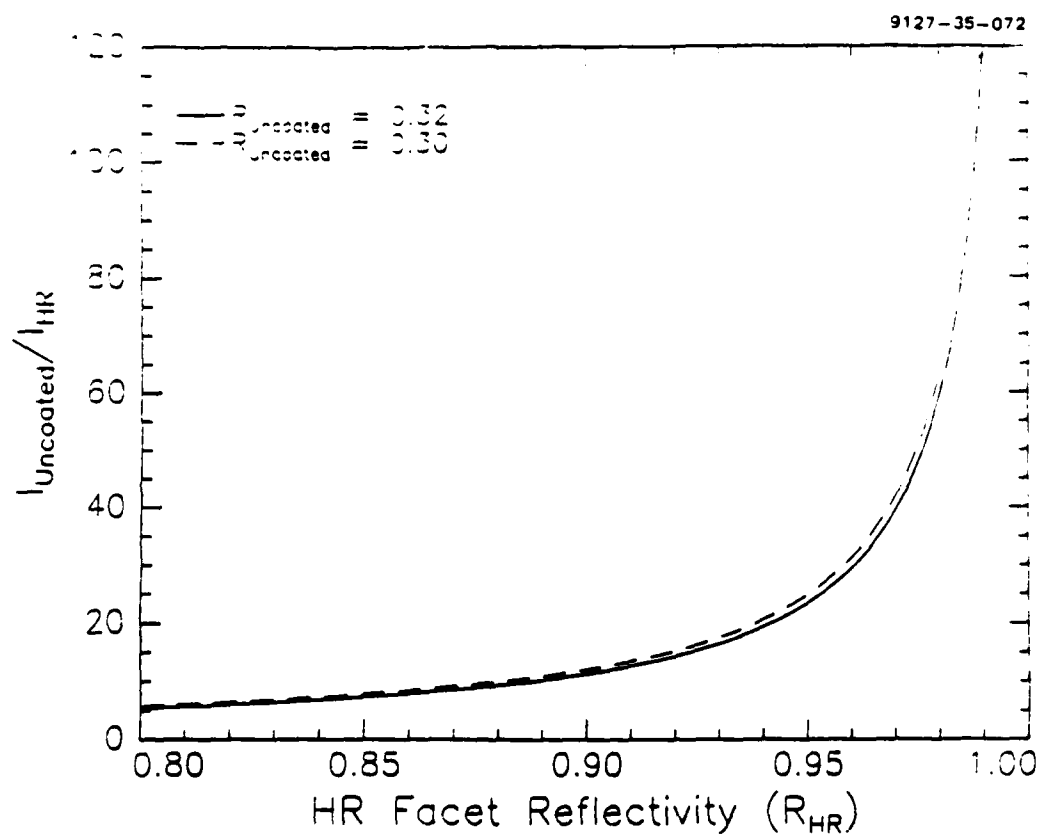


Figure 16. Output power ratio for the uncoated and HR coated facets of a cleaved facet GaAs/GaAlAs diode laser as a function of the HR facet reflectivity. Results are shown for uncoated facet reflectivities of 0.30 + 0.32. Curves are based on Eq.(4) which is valid for lasers with Fabry-Perot resonators.

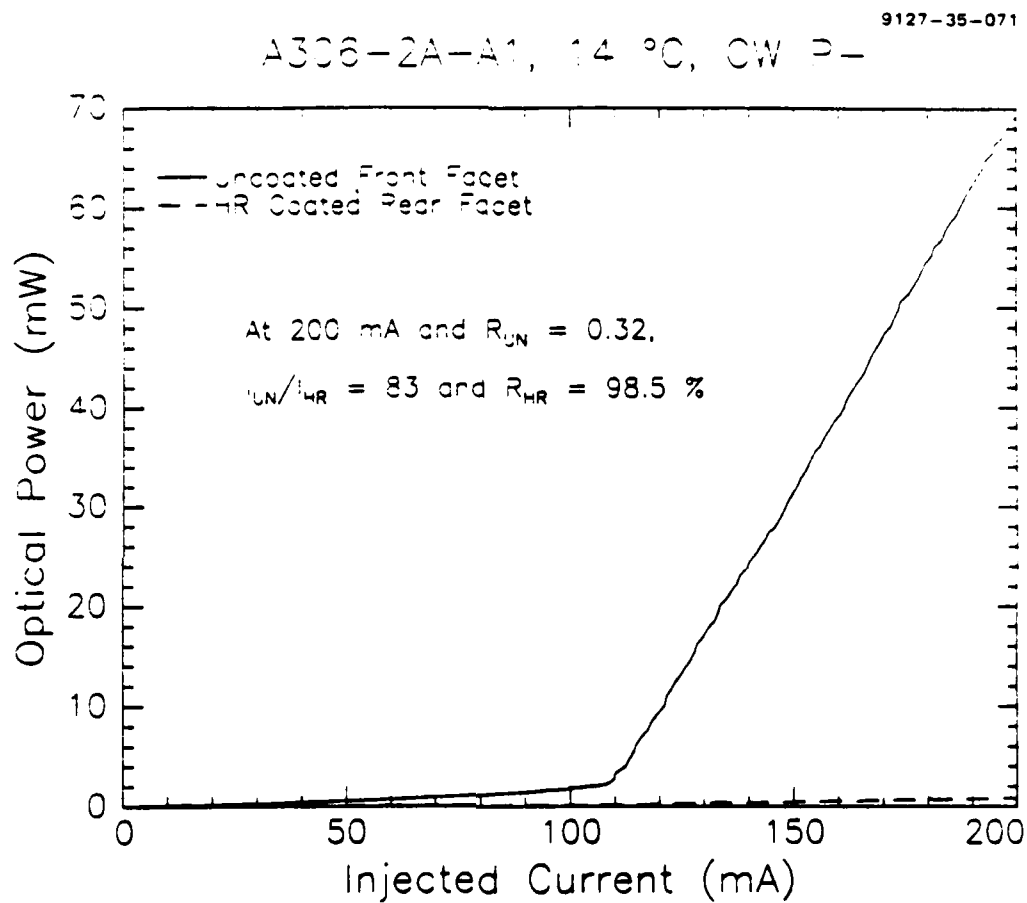


Figure 17. CW P-I data for diode A306-2A-A1 after one facet was coated for high reflectivity. The intensity ratio of the output powers from the uncoated and HR facets at 200 mA are used with Eq.(4) to calculate a HR facet reflectivity of 98.5%

facets at 200 mA was 83, corresponding to a typical HR facet reflectivity of 98.5%. Also note the shift to lower threshold current after HR coating.

### 3.5.2 Anti-Reflection (AR) Coated Facets

The vast majority of AR coatings performed for this contract used a single-layer dielectric film deposited in a high vacuum system by E-beam evaporation. Single-layer AR coatings are the easiest to analyze theoretically,<sup>15</sup> and simplest to fabricate and analyze. Early in the program we explored 2-layer AR coatings ( $\text{Al}_2\text{O}_3/\text{ZrO}_2$ ), but quickly abandoned that effort to develop a reproducible single-layer technique. The AR coating goal, as originally stated in Section 2, was extremely low facet reflectivities of  $\sim 1 \times 10^{-4}$ . Our AR coating technology was developed synergistically under this contract, and USAF Contract #F29601-87-C-0029. The resulting technology was used to provide our best AR coatings to amplifiers fabricated for this project.

The lowest possible reflectivity from a single-layer AR coated surface for monochromatic plane-wave radiation normally incident on the surface occurs when two conditions are satisfied. First, the refractive index of the AR coating ( $n_{\text{AR}}$ ) is chosen to equal the square root of the substrate refractive index ( $n_s$ ),

$$n_{\text{AR}} = n_s^{1/2} \quad (5)$$

This assumes that the AR coating is bordered by air with a refractive index of 1. Secondly, the thickness of the AR coating ( $d_{\text{AR}}$ ) must match the following equation,

$$d_{\text{AR}} = \lambda(2m-1)/(4n_{\text{AR}}), \quad m = 1, 2, 3, \dots \quad (6)$$

Normally  $m$  is one, and the film is designated a quarter-wave coating. A film conforming exactly to the above criteria has zero reflectivity at a single wavelength. Reflectivity increases for changes in wavelength, deviations in refractive index or thickness and non-normally incident radiation.

In practice even the two criteria for a high quality single-layer AR coating are difficult to meet. The effective refractive index of the GaAs/GaAlAs laser/amplifier facets, a fundamental quantity in establishing AR coating parameters, is not known exactly for each new epitaxial growth. Uncertainty in the effective index results from the dependence of index on the complicated graded index (GRIN) waveguide and single quantum well regions of the amplifiers which are not necessarily identical between epitaxial growths. Variability in effective index also requires variability in the AR coating index, if the lowest facet reflectivities are to be obtained. Also, light

generated by a diode laser does not satisfy the plane wave assumption of the previous paragraph. Large deviations from plane-wave reflectivities occur when the optical mode size resulting from the GRIN waveguide approaches the wavelength of light in the diode.<sup>10</sup> This is essentially a diffraction effect causing a large percentage of the light to strike the facet/coating at non-normal incidence.

Because of the uncertainty in identifying the optimal refractive index for the AR coating, we choose AR coating materials and a deposition technique that allowed variation of the film index. As an initial approximation for the GaAs/GaAlAs waveguide index of refraction, we used the group refractive index ( $n_G$ ) of lasers fabricated from amplifier epitaxial material. The group index can be calculated from the measured wavelength difference ( $\Delta\lambda$ ) between successive longitudinal modes of the Fabry-Perot resonator,<sup>16</sup>

$$\Delta\lambda = \lambda^2 / (n_e - \lambda dn_e / d\lambda) 2L, \quad (7)$$

where  $n_e$  is the waveguide effective index and  $L$  the resonator length. We observed variations in  $n_G$  between 3.4 and 4.0 for our 500- $\mu\text{m}$ -long diodes with wavelength between 820 and 840 nm and  $\Delta\lambda$  between 0.17 and 0.21 nm.

The range of  $n_G$  suggested AR coating materials with indices between 1.84 and 2.00. At the suggestion of Charles Carniglia, an Air Force consultant, we initiated single-layer coatings with scandium oxide ( $\text{Sc}_2\text{O}_3$ ). We utilized E-beam evaporation with variable oxygen background pressure to adjust the film refractive index. Later in the program we also used E-beam evaporated hafnium oxide ( $\text{HfO}_2$ ).

We optimized the AR coating refractive index for each epitaxial growth by systematically varying the refractive index for the first set of amplifiers fabricated from that particular growth. The AR coating thickness was automatically optimized for each deposition, regardless of refractive index, by our *in situ* monitoring technique which utilized the shift of laser threshold current as a function of film thickness. During the AR coating process the laser was operated under pulsed conditions, and the deposition was stopped when the threshold current reached its maximum value. The resulting amplifiers had the best possible suppression of self-oscillation given AR film composition. The use of phase sensitive detection in conjunction with pulsed laser operation allowed discrimination between the optical signals from the diode and background from the E-beam process.

The reflectivity of our AR coated amplifier facets was evaluated with two techniques that are derivatives of the method developed by Hakki and Paoli<sup>17</sup> for measuring net gain in Fabry-Perot

resonators. The work of Hakki and Paoli relates the single pass gain ( $G_S$ ) in a Fabry-Perot resonator to the facet reflectivities ( $R_i$ ) and the ratio of adjacent maxima ( $P_{\max}$ ) to minima ( $P_{\min}$ ) of the spontaneous emission longitudinal mode spectrum ( $\rho = P_{\max}/P_{\min}$ ),

$$G_S \equiv e^{(g-\alpha)L} = (R_1 R_2)^{-1/2} (\rho^{1/2} - 1) / (\rho^{1/2} + 1). \quad (8)$$

Here  $g$  is the small signal gain,  $\alpha$  the distributed optical loss and  $L$  the cavity length. At laser threshold  $\rho$  approaches  $\infty$  and the above equation reduces to,

$$G_S^{\text{Th}} = (R_1 R_2)^{-1/2}. \quad (9)$$

For an uncoated device, facet reflectivities are known to be 32%, so  $G_S^{\text{Th}}$  is 3.12. After coating, measurement of  $\rho$  at the uncoated laser threshold allowed the calculation of the AR reflectivity ( $R_{\text{AR}}$ ) from Eq. (8) rewritten in the form,

$$R_{\text{AR}} = (R_{\text{HR}} G_S^2)^{-1} (\rho^{1/2} - 1)^2 / (\rho^{1/2} + 1)^2, \quad (10)$$

if the HR facet reflectivity ( $R_{\text{HR}}$ ) is known and the single pass gain did not change.

We applied the above technique to determine amplifier AR facet reflectivities in two different ways. In the first, which we will refer to as the spontaneous emission method, the spontaneous emission from the AR facets of amplifiers operating CW at their uncoated threshold currents was focused onto the entrance slit of a 3/4 meter monochromator. The resulting spectra were used to extract  $\rho$  near the maximum wavelengths of amplifier gain, and the  $\rho$ 's were plugged into Eq. (10) to generate  $R_{\text{AR}}$ . A typical spectrum is shown in Figure 18.

The 2-pass MOPA technique was the second method for determining amplifier AR facet reflectivities. A chopped beam from a master oscillator was injected into an amplifier operating CW at the original uncoated laser threshold current. The magnitude of the master oscillator signal after amplification was obtained by phase sensitive detection.  $\rho$  was obtained by recording the amplified part of the master oscillator signal as a function of substrate temperature. Derivation of the relationship between  $\rho$ ,  $G_S$  and reflectivities requires consideration of a reflection Fabry-Perot resonator rather than the transmission Fabry-Perot used to obtain Eq. (10), and results in the following relationship:

$$\rho = [(1 + (R_1 R_2)^{1/2} G_S) / (1 - (R_1 R_2)^{1/2} G_S)]^2 [(R_1^{1/2} - R_2^{1/2} G_S) / (R_1^{1/2} + R_2^{1/2} G_S)]^2 \quad (11)$$

9027-35-07

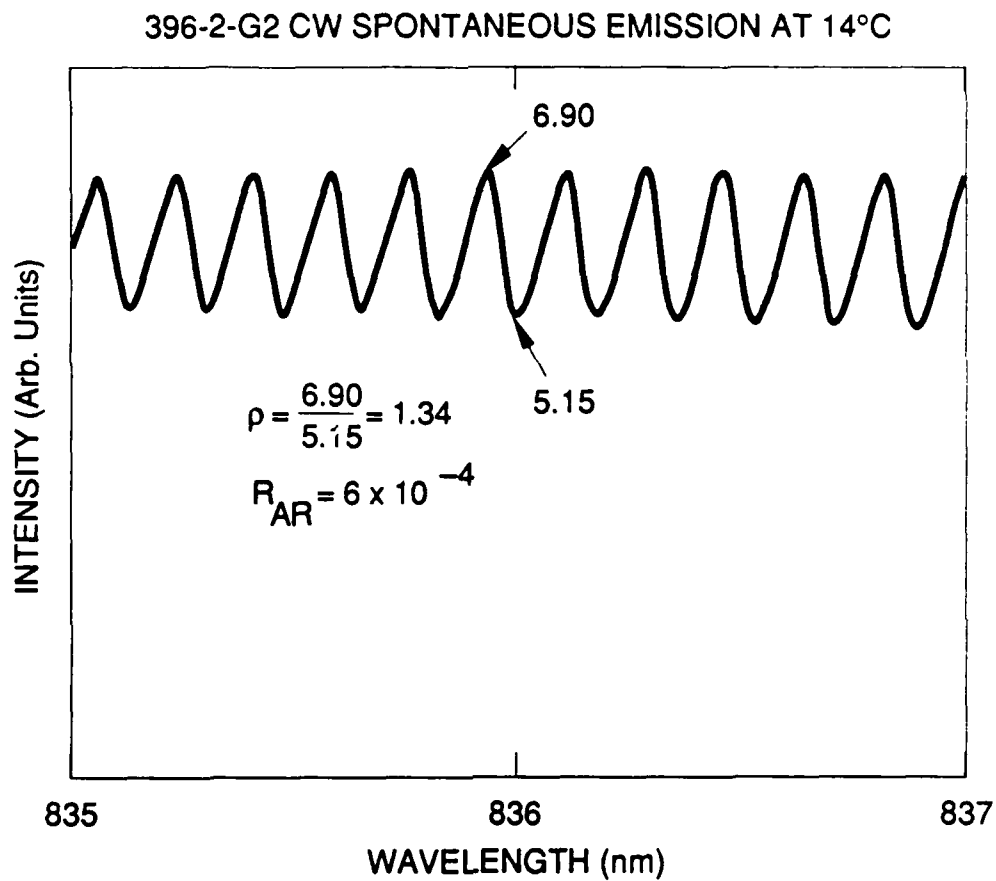


Figure 18. Spontaneous emission spectrum from amplifier 396-2-G2 operating CW at 105 mA and 14°C.  $R_{AR}$  calculated from Eq. (10).



Sample data for the 2-pass MOPA technique are shown in Figure 19. The determination of  $R_{AR}$  is complicated by the mutual dependence of gain and resonator length on temperature.<sup>18</sup> The effect of thermally induced changes in gain can be minimized by drawing straight lines through the amplified MO power maxima and minima, and using those lines to generate  $\rho$  at the desired temperature. This procedure is also shown in Figure 19.

Comparing the two methods of determining the AR facet reflectivity, we expect the spontaneous emission method to yield the smaller value of  $\rho$  and therefore  $R_{AR}$ . This conclusion is based on the fact that the spontaneous emission method includes light that has no chance to multi-pass in the resonator. This light is spontaneous emission that originates traveling toward the AR facet, but at a large enough angle so that upon reflection off the AR facet it does not remain in the pumped gain region. The additional background radiation is added to both the peaks and valleys of the resonator longitudinal modes, and decreases  $\rho$ . The 2-pass MOPA method only counts light that is injected into the resonator optical mode, and therefore has the correct trajectory to remain in the gain region. This difference can lead to a rather large discrepancy in the calculated facet reflectivity as demonstrated by Figures 18 and 19. For the same amplifier the spontaneous emission method results in an AR facet reflectivity of  $6 \times 10^{-4}$ , while the 2-pass MOPA results indicate a value of  $9.9 \times 10^{-3}$ .

We have encountered one major problem with our AR coating technique which seems to be caused by aging of the AR films with time. Figure 20 depicts optical power emitted from the AR coated facet of a single amplifier as a function of injected current (P-I). Data are shown after AR coating with the amplifier in the deposition system both before breaking vacuum and after the introduction of air. Upon breaking vacuum, and introducing air to the amplifier facets, we usually saw a shift to lower threshold current indicating higher reflectivity on the AR facet. This shift was observed with  $\text{Sc}_2\text{O}_3$  and  $\text{HfO}_2$  single layer AR coatings. Shifts to lower threshold current were also observed as a function of amplifier operating time. These shifts are most likely due to oxidation of the AR coatings which changes both the thickness and refractive index of the films.

The aging phenomenon observed in our AR coatings could probably be arrested by depositing the films at elevated temperatures, but that precludes use of our threshold current shift *in situ* monitoring technique. It also fixes the film index at one value which may not produce a low enough facet reflectivity. A multiple-layer AR coating technique at elevated temperature might provide a stable, low reflectivity alternative.

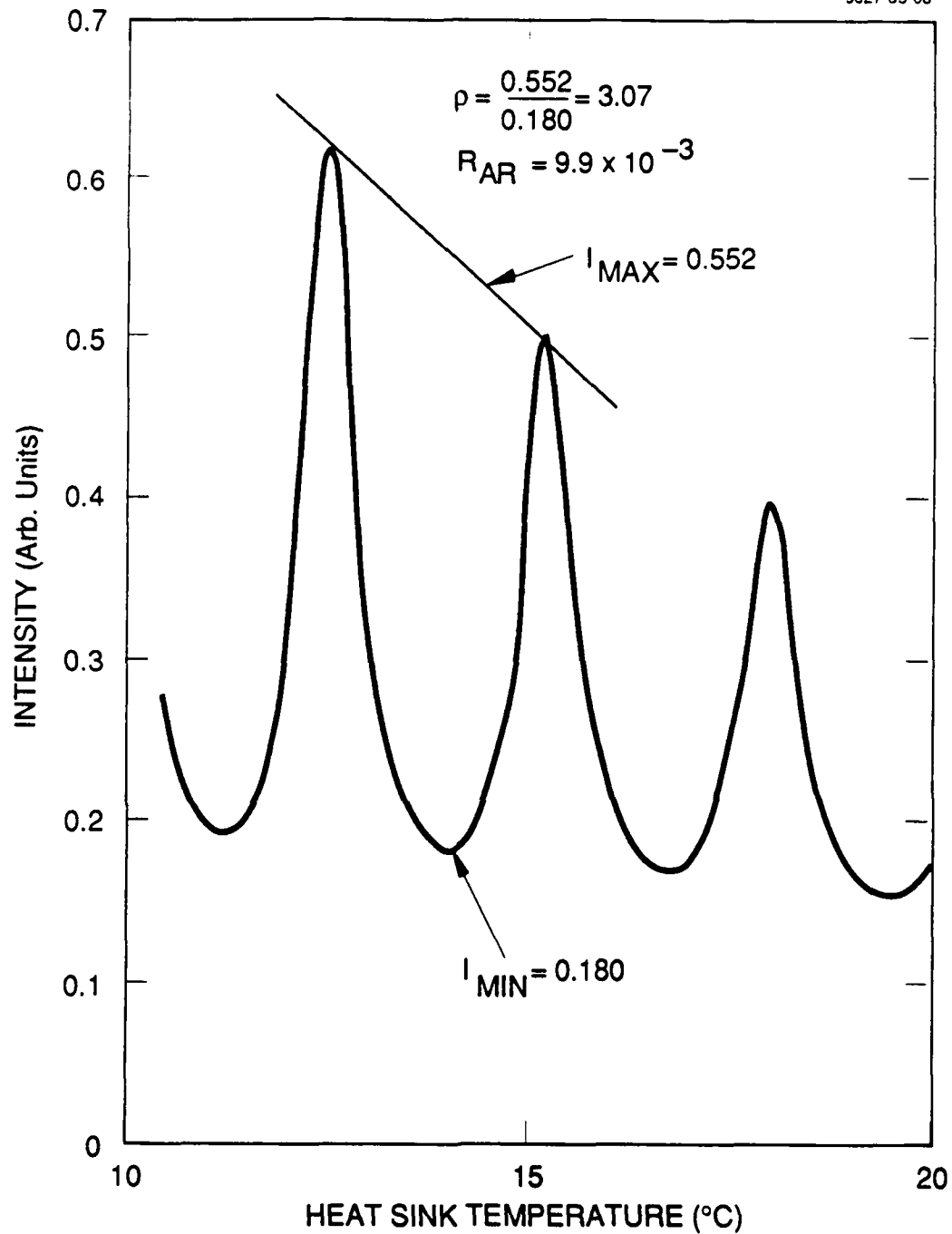


Figure 19. 2-Pass MOPA technique for determining AR coated facet reflectivity ( $R_{AR}$ ). Amplifier 396-2-G2 operating at 104 mA with  $\sim 0.2 \mu\text{W}$  of unjected light at 833.5 nm.

9027-35-09

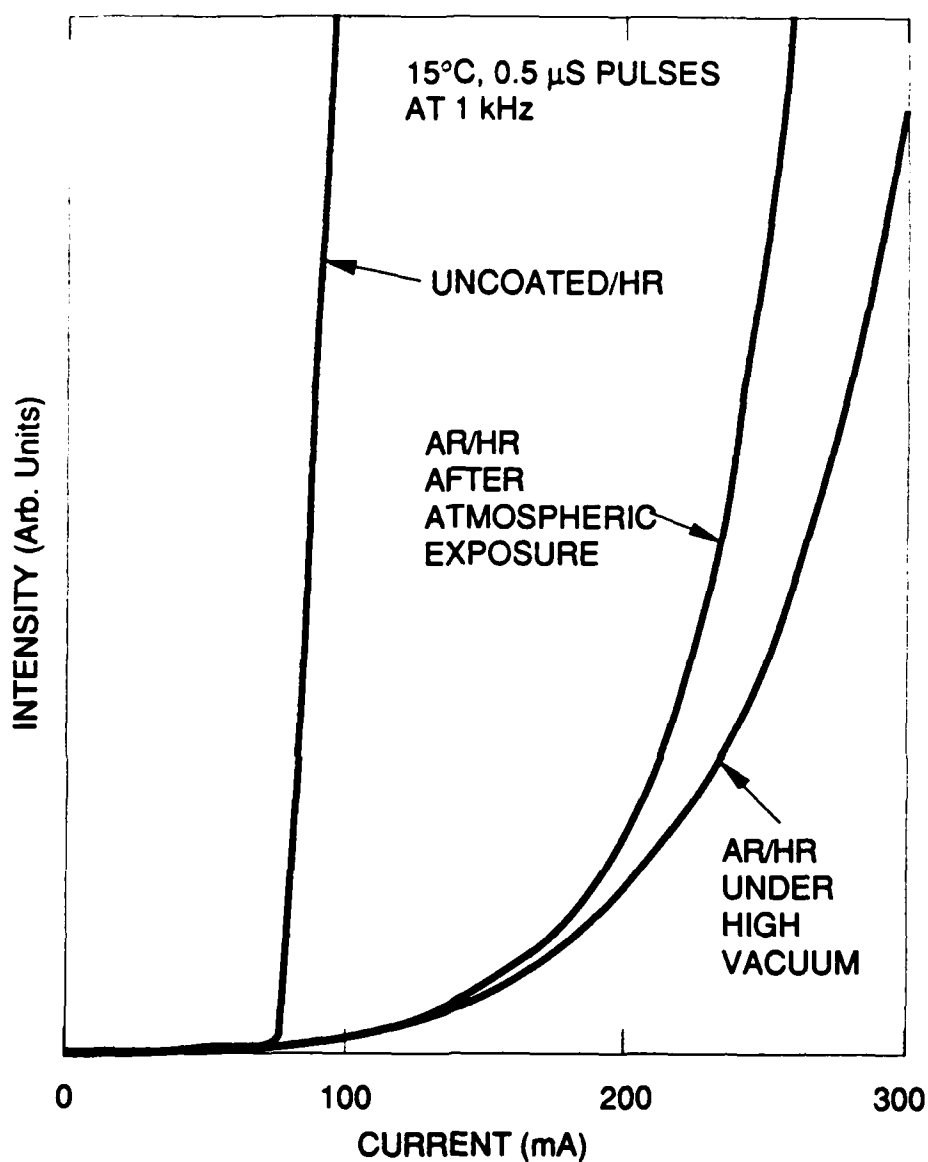


Figure 20. P-I data for diode 396-2-G2 before AR coating, and after AR coating both under high vacuum and after atmospheric exposure. Data were taken at 15°C with 0.5 μs pulses at 1 kHz.

### 3.6 AMPLIFIER BURN-IN AND TESTING

After AR coating, the amplifiers received a 2-hour burn-in with a current of 200 mA. The devices were monitored throughout the fabrication process by obtaining power versus current (P-I) data. P-I plots were a convenient way to monitor the effects of the various coating stages, and, for the multiple amplifiers on the test bars, to quickly obtain statistics regarding amplifier-to-amplifier uniformity and failure mechanisms.

We recorded the optical emission by using a lens (Melles Griot 06 GLC 002) to image the output facet onto a calibrated detector. The P-I data were obtained pulsed before heatsink bonding, and cw at various stages after bonding: before any optical coating, after HR coating, after AR coating, and after the 2 h burn-in. Only the facets eventually AR coated were tested. In some cases amplifiers were processed with electrically isolated p-type contacts before bonding. Pulsed P-I data for these devices utilized no imaging; the detector was placed within 1 mm of the output facet and captured virtually all of the emitted radiation.

We now present two sets of P-I plots for representative amplifiers from two different material growths designated as A306 and A46. Figure 21 shows P-I data for an A306 amplifier obtained after all the crucial fabrication stages outlined above. Figure 22 shows P-I data for an amplifier fabricated from A46 material. The curves for both devices are similar and clearly show the decrease in laser threshold current after HR coating, the suppression of laser output after AR coating, and an apparent degradation of the AR coating after burn-in. Both of these amplifiers subsequently underwent optical testing in our MOPA apparatus and were found to have AR facet reflectivities of  $1.7 \times 10^{-3}$  (A306-2A-E5) and  $9.3 \times 10^{-3}$  (A46-D3-G10).

A number of 11-element test bars were also fabricated from the A306 and A46 material under USAF contract F29601-87-C-0029 for inclusion in a 2-D PC MOPA system delivered to AFWL in December 1990. Test results from these amplifier arrays are of interest because they give insight into failure modes and fabrication yields of our processing techniques. Individual diodes in the test bars exhibited dramatic reductions in optical power at a given injection current as function of cw operating time. In one A306 bar failures were clearly due to poor diode to heatsink bonding. In other bars fabricated from MOVPE growth A306, we identified no clear failure mechanism. In six A306 bars with good heatsink bonds we observed seven failures out of a total of 66 diodes. Our best estimate is that failures were caused by dark-line defects incorporated during the growth or introduced during processing. Some of the failures in amplifiers fabricated from A46 MOVPE material also seemed to be due to dark-line defects. In addition, I-V data indicate that failures were caused by electrical shorts that developed across some of the diodes. Because the diode facets

9127-43-19

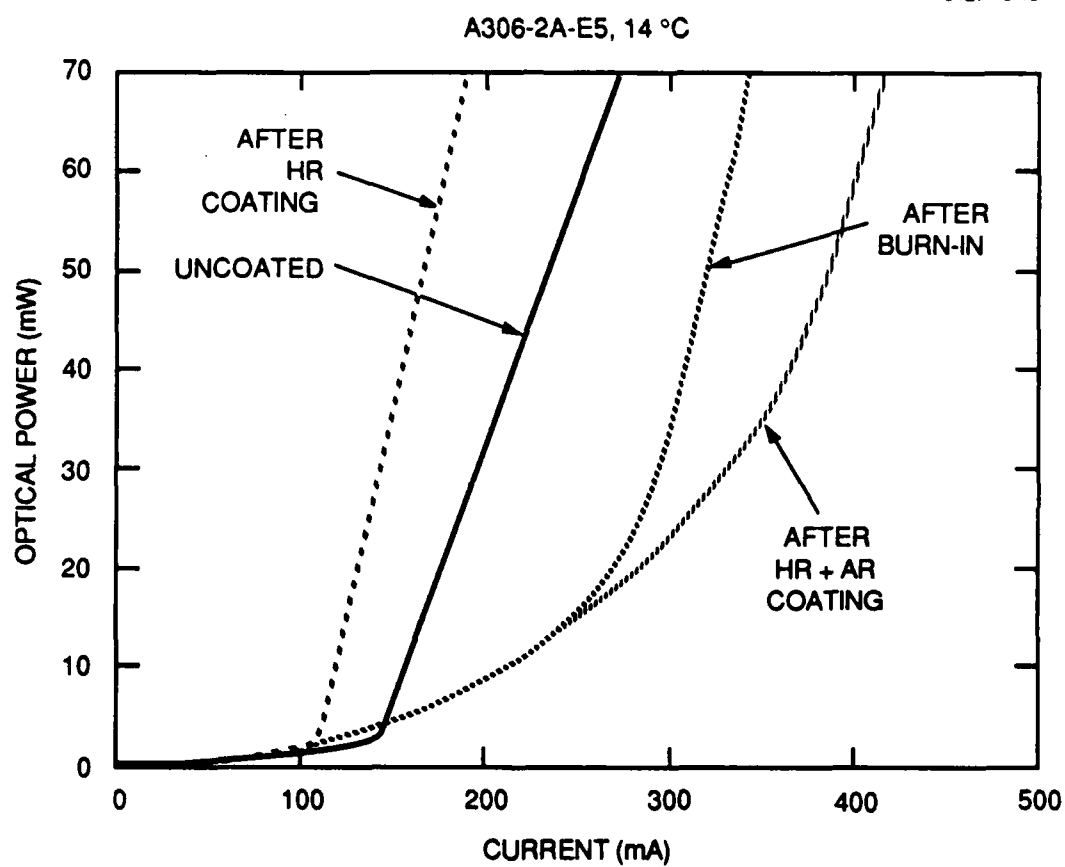


Figure 21. CW P-I data for A306-2A-E5 at various stages of fabrication.

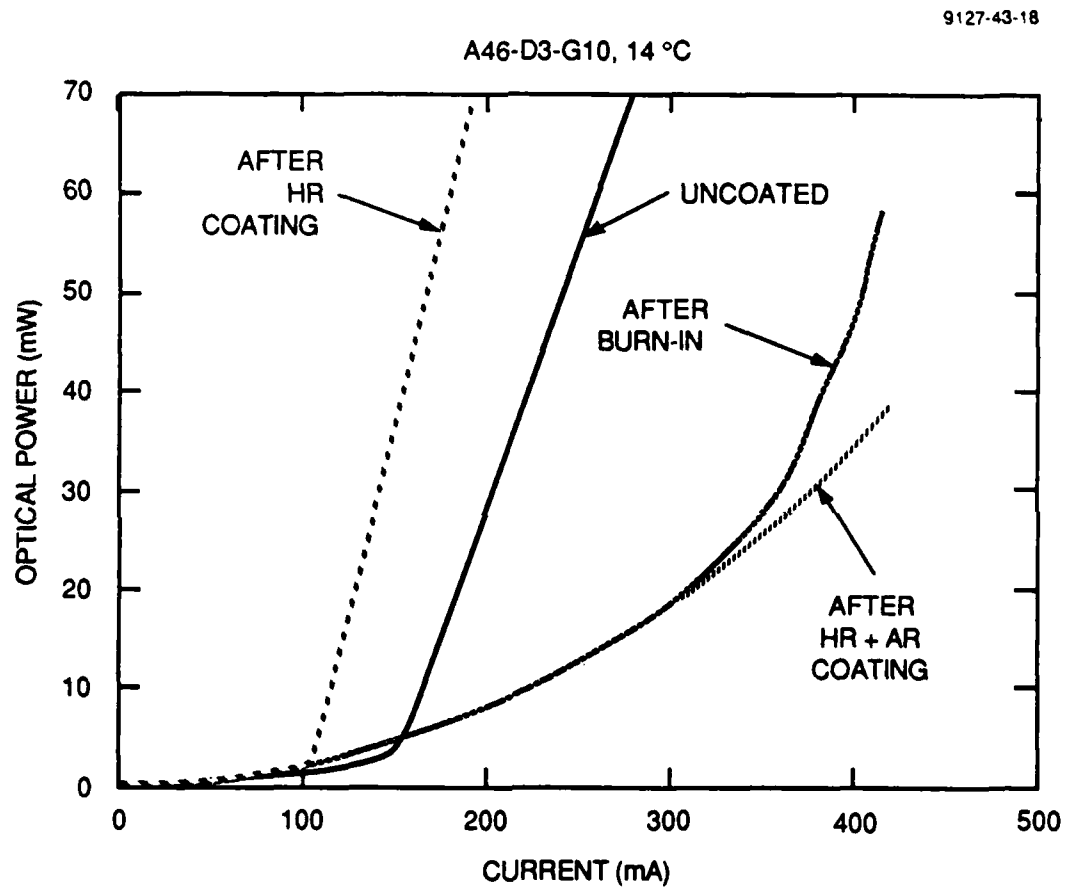


Figure 22. CW P-I data for A46-D3-G10 at various stages of fabrication.

were passivated with dielectric optical coatings, we speculate that the shorts developed across the SQW active regions.

We have also noted that, with the exception of diodes that failed, the uniformity of P-I characteristics for diodes remained relatively constant through the HR coating step of the fabrication sequence. This statement is true for five of six bars made from A306 material. Uniformity deterioration in the sixth test device was the result of poor bar to heatsink bonding.

Application of AR coatings seems to increase diode P-I nonuniformity within an array. However, the AR coatings increase diode laser threshold currents and suppress optical output. This effectively expands scales on P-I plots and makes it difficult to compare uniformity with HR only and uncoated devices. Any increases in diode performance nonuniformity by the AR coating were probably due to nonuniformities in the refractive index or thickness of the coatings. We attempted to insure good uniformity in our dielectric coatings by maintaining a very clean deposition system and utilizing a large source to substrate separation.

## SECTION 4

### AMPLIFIER CHARACTERIZATION

#### 4.1 TWO PASS MOPA CHARACTERISTICS

##### 4.1.1 Operative Processes and Expected Gain

The amplifiers fabricated on this program are designed to work in a four-pass PC MOPA as shown in Figure 4 of Section 2. As a result, the back facet is high reflection (HR) coated, and all MOPA measurements must be made with the MO beam passing twice through the gain medium. In effect, this simulates the first half of the four-pass PC MOPA amplification sequence.

Figure 23 shows the basic arrangement of a two-pass, single-end-coupled MOPA. Just below the amplifier drawing is a plot of the beam intensities in the two MO passes ( $I_1(x)$  and  $I_2(x)$ ) and gain coefficient ( $g(x)$ ) along the propagation direction ( $x$ ) of the amplifier which has a length ( $L$ ). Light from both passes are inside the amplifier simultaneously and thus saturate the gain with a total intensity profile that is non-uniform in the  $x$  direction. The situation is further complicated by the presence of amplified spontaneous emission (ASE) which also varies with  $x$  and further contributes to gain saturation. Feedback from the AR coated facet can also contribute significantly to gain saturation and other undesirable effects (such as parasitic oscillation) if the gain-reflectivity product,  $G_S(R_1R_2)^{1/2}$ , approaches unity. Here  $R_1$  is the AR coated facet reflectivity,  $R_2$  is the HR coated facet reflectivity, and  $G_S$  is the single pass gain.

A computer model is required to solve for the MOPA output power because of the gain saturation by multiple sources and the dependence on  $x$  of all intensities. HRL has developed a PC MOPA output power computer model that can also treat single pass MOPAs, double pass MOPAs, and lasers. The computer code propagates an assumed input intensity down the amplifier which is divided into 100 segments of length  $\delta x = L/100$ . The diode amplifier gain is assumed to be homogeneously broadened and thus satisfies the equation for  $g(x)$  shown at the right of Figure 23.  $I_T(x)$  is the total intensity from all sources:  $I_T(x) = I_1(x) + I_2(x) + ASE(x) + I_{AR}(x)$ . Here  $ASE(x)$  is the ASE intensity, and  $I_{AR}(x)$  is the the intensity due to feedback reflections off the AR coated facet.  $I_{SAT}$  is the saturation parameter and  $g_0$  is the small-signal gain coefficient.

The effects of ASE are included by adding an ASE seed power into each amplifier segment that is proportional to the saturated gain in that segment. Scaling the ASE seed to an assumed ASE gain limit is accomplished by running the model with no MO input and zero facet reflectivity. The double-pass ASE limit is assumed to be 40 dB, in agreement with previous DH



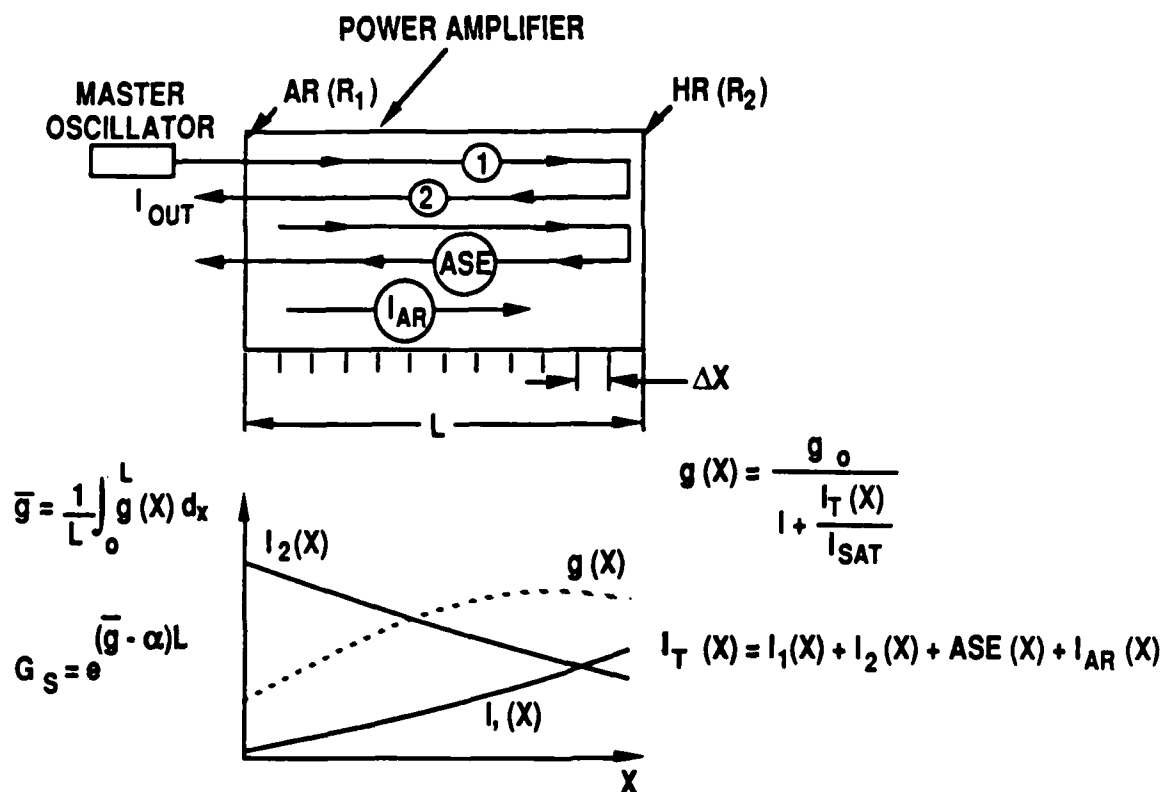


Figure 23. Two-pass, single-end-coupled MOPA.

single stripe amplifier work.<sup>19</sup> The model propagation process is iterated until a stable convergence is obtained to within 1% for both the total intensity and the saturated gain coefficient.

Modeling results for the integrated gain-length product as a function of drive current for the two pass MOPA is shown in Figure 24 for several hypothetical operating conditions. The integrated gain-length product is the quantity  $(g(x) - \alpha)dx$  integrated over the length L of the amplifier, where  $\alpha$  is the distributed loss coefficient. The small signal product is shown in all cases. The top dashed line corresponds to no ASE and no feedback from the AR coated facet being present. In this case the gain-length product varies linearly with drive current as expected.

If the effects of ASE are added while keeping R<sub>1</sub>=0 (solid line), the gain-length product is observed to saturate at the higher currents. At the higher currents the gain becomes so high that a significant fraction of the population inversion is extracted by the initially weak spontaneous emission in just two passes of the amplifier. Thus even with a perfect AR coated facet, the gain

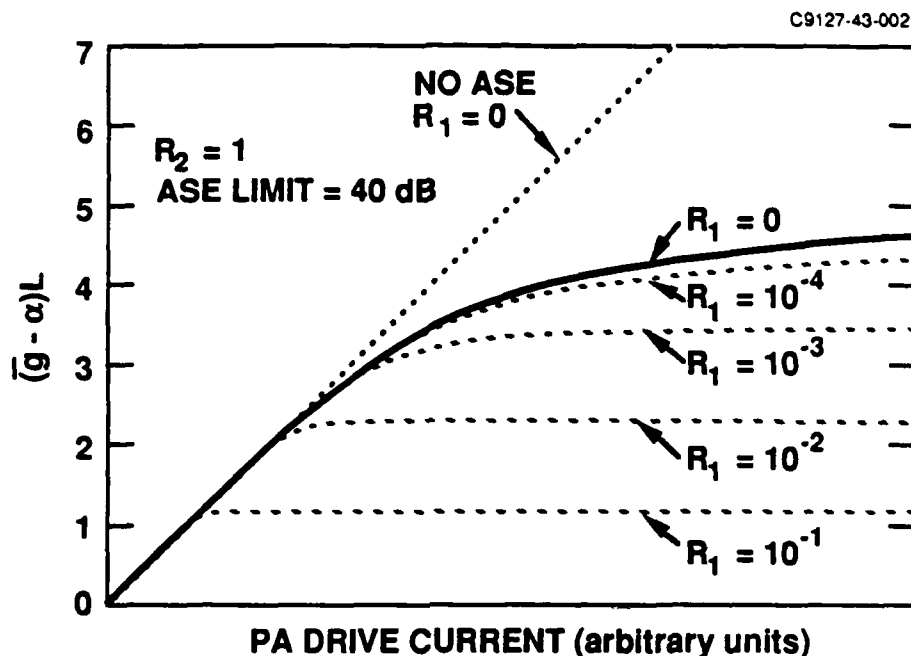


Figure 24. Gain length product dependence on ASE and feedback.

can not exceed a certain limiting value. The ASE limit on integrated gain-length product seen in the figure is about 4.6, corresponding to the initially assumed double-pass gain limit of 40 dB. Even though the gain is partially depleted by the ASE, the device has no feedback and thus will still function well as a conventional traveling-wave amplifier.

The lower dashed lines in Figure 24 correspond to cases where both ASE and non-zero AR coated facets are present. In these cases, feedback from the facet eventually causes the amplifier to oscillate. For the higher reflectivities ( $R_1 = 10^{-1}$  and  $10^{-2}$ ), the laser threshold is well-defined by the sudden change in slope of the curves and the clamping of the gain at the laser threshold value given by  $G_S = (R_1 R_2)^{-1/2}$ . For the lower reflectivities ( $R_1 = 10^{-3}$  and  $10^{-4}$ ), the laser threshold is not well defined, and clearly defined gain clamping and laser action occur only at very high currents.

The amplifier is lasing once the curves become horizontal at the highest currents. At lower currents between the horizontal and the  $45^\circ$  angled portions of the curves the device is operating as a Fabry-Perot amplifier. This mode of operation exhibits characteristics that are midway between traveling-wave amplifier and laser. The device isn't lasing, but feedback from the AR coated facet coherently interferes with the MO input to produce resonances in the observed gain. The resonances are highly dependent on MO wavelength and other operating parameters.

Regions of strong resonances must be avoided in PC MOPA applications because aberrations present inside a resonator can not be corrected by an externally located phase conjugate mirror.

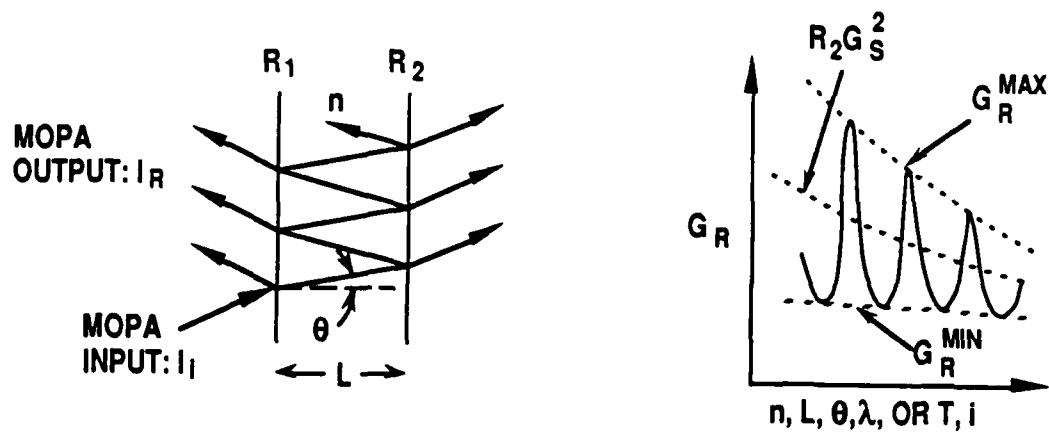
#### 4.1.2 Fabry-Perot Resonator Effects

A diagram of a Fabry-Perot amplifier is shown in Figure 25 along with parameter definitions and expressions for observed gain ( $G_R$ ) and resonance strength ( $\rho_R$ ). Fabry-Perot amplifiers can be operated in either the transmission mode where light passes through the amplifier, or in the reflection mode where the amplified light reflects back toward the MO. Our measurements are concerned with reflection mode operation since the back amplifier facet is HR coated with  $R_2 \equiv 1$ . The expressions for reflection mode  $G_R$  and  $\rho_R$  shown in the figure are derived by summing up the amplitudes and phases of the amplified multiple reflections between the amplifier facets.

Resonances in the observed gain  $G_R$  occur when the single pass phase shift ( $\delta/2 = 2\pi nL \cos(\theta)/\lambda$ ) equals an integer multiple of  $\pi$ . Here  $n$  is the refractive index of the amplifier medium,  $L$  is the amplifier length,  $\theta$  is the interior tilt angle of the MO beam, and  $\lambda$  is the MO wavelength. The strength of the resonance is determined by the quantity  $1 - G_S(R_1 R_2)^{1/2}$  which appears in the denominators of both  $G_R$  and  $\rho_R$ . When  $G_S(R_1 R_2)^{1/2} = 1$  the expressions go to infinity and the amplifier becomes a laser. The resonances become longitudinal laser modes. For values less than but close to one, the observed gain and the resonance strength can be very large. Only when  $R_1 = 0$  do the resonances disappear and the observed gain becomes  $G_R = R_2 G_S^2$ .

In our 500- $\mu\text{m}$ -long amplifiers which operate near 830 nm we observe the resonances to be spaced about 0.17 nm apart. Thus a change in MO wavelength of about one part in 5000 will produce a shift from one resonance to another, or a change of one part in 10,000 will shift from a peak to a valley. The single pass phase shift,  $\delta/2$ , is dependent on  $n$ ,  $L$ , and  $\cos(\theta)$  as well as wavelength. Thus changes in any of these quantities by one part in 10,000 will also shift the observed gain from a peak to a valley. Since  $n$  and  $L$  are functions of device temperature ( $T$ ), and since  $n$  is also a function of drive current ( $i$ ), changes in  $T$  and  $i$  will also cause the resonance pattern to shift. When operating at a fixed MO wavelength we therefore expect to see resonances in the MOPA output power as the drive current and device temperature are varied.

The resonance shift with temperature is particularly useful in obtaining accurate measurements of the AR coated facet reflectivity, as has been discussed in Section 3. Facet reflectivity measurements will be discussed again later in this section, as will MOPA output power measurements which clearly show the effects of Fabry-Perot resonances.



$$G_S = e^{(g - \alpha)L}$$

$\delta = \text{DOUBLE PASS PHASE SHIFT}$

$$G_R \equiv \frac{I_R}{I_i}$$

$$\delta = \frac{4\pi nL \cos\theta}{\lambda_0}$$

$$G_R = \frac{(\sqrt{R_1} - \sqrt{R_2} G_S)^2 + 4\sqrt{R_1 R_2} G_S \sin^2\left(\frac{\delta}{2}\right)}{(1 - \sqrt{R_1 R_2} G_S)^2 + 4\sqrt{R_1 R_2} G_S \sin^2\left(\frac{\delta}{2}\right)} ; \begin{cases} \text{MAX AT } \frac{\delta}{2} = m\pi \\ \text{MIN AT } \frac{\delta}{2} = \left(m + \frac{1}{2}\right)\pi \\ \text{WHEN } G_S > \frac{1}{\sqrt{R_2}} \end{cases}$$

$$P_R \equiv \frac{I_R^{\text{MAX}}}{I_R^{\text{MIN}}} = \left( \frac{1 + \sqrt{R_1 R_2} G_S}{1 - \sqrt{R_1 R_2} G_S} \right)^2 \cdot \left( \frac{\sqrt{R_1} - \sqrt{R_2} G_S}{\sqrt{R_1} + \sqrt{R_2} G_S} \right)^2 ; \text{ FOR } G_S > \frac{1}{\sqrt{R_2}}$$

Figure 25. Reflection-mode Fabry-Perot amplifier.

## 4.2 AMPLIFIER PARAMETER EVALUATION FROM MOPA MEASUREMENTS

### 4.2.1 MOPA Measurements Apparatus

The two-pass MOPA apparatus used for optical characterization of the amplifiers is shown in Figure 26. The apparatus is used to measure small signal gain, coupling efficiency, AR coated facet reflectivity, MOPA output power, and beam quality. A 15-mW master oscillator (MO) is passed through a pair of 30-dB optical isolators to suppress any potential optical feedback induced instabilities. The MO operates on a single longitudinal mode and has a diffraction-limited output. An optical attenuator is employed during gain, facet reflectivity, and coupling efficiency measurements to reduce the MO intensity to microwatt levels. This prevents saturating the amplifier gain. The half-wave plate following the attenuator is used to rotate the MO polarization so that both TE and TM gain may be evaluated.

A set of adjustable beam forming optics is used to tailor the MO beam shape to match the requirements of two different final focusing lenses which couple power into the amplifier. The operation of these lenses is shown in Figure 27. Both lenses produce beams that are focused perpendicular to the diode junction (small amplifier dimension) and that are collimated in the other (100  $\mu\text{m}$ ) dimension. This provides maximum power coupling into the amplifier and complete filling of the gain medium.

After amplification a portion of the MOPA output is coupled out of the system by a nonpolarizing beamsplitter into a power meter. A fraction of the output is also directed to a series of lenses and a galvanometer mirror profile scanner which are used to measure the near- and far-field output intensity distributions of the MOPA. A chopper and lock-in amplifier are also used to synchronously detect the MOPA output. Signal to noise enhancement is required in order to detect the MOPA signals during small-signal gain, coupling efficiency, and facet reflectivity measurements. In these instances the MOPA power is typically three orders of magnitude smaller than the spontaneous emission. Synchronous detection is also employed during high power MOPA measurements since it effectively eliminates the spontaneous emission component.

During gain measurements a logarithmic amplifier is connected to the lock-in output. The log amp output is applied to the y-axis of an x-y recorder, and a signal proportional to the amplifier drive current is applied to the x-axis. After careful calibration of the optical losses, this arrangement allows us to record the gain-length product as a function of amplifier drive current directly onto the x-y chart with no intermediate data reduction.

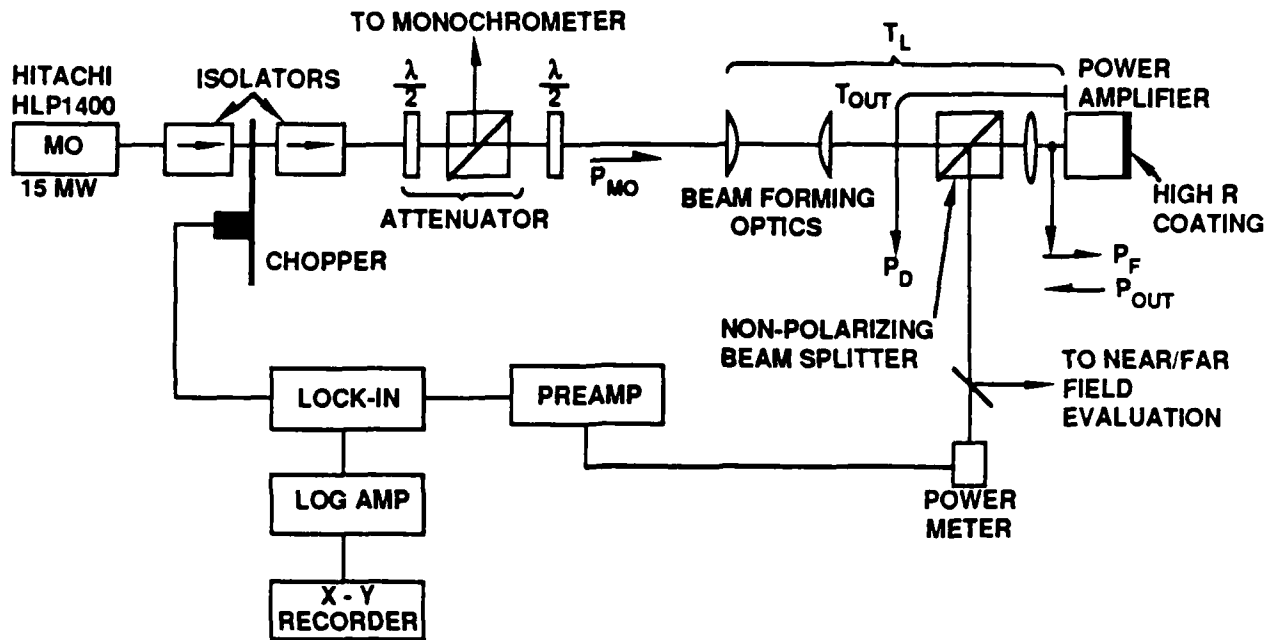


Figure 26. Apparatus for MOPA measurements.

C9127-43-005

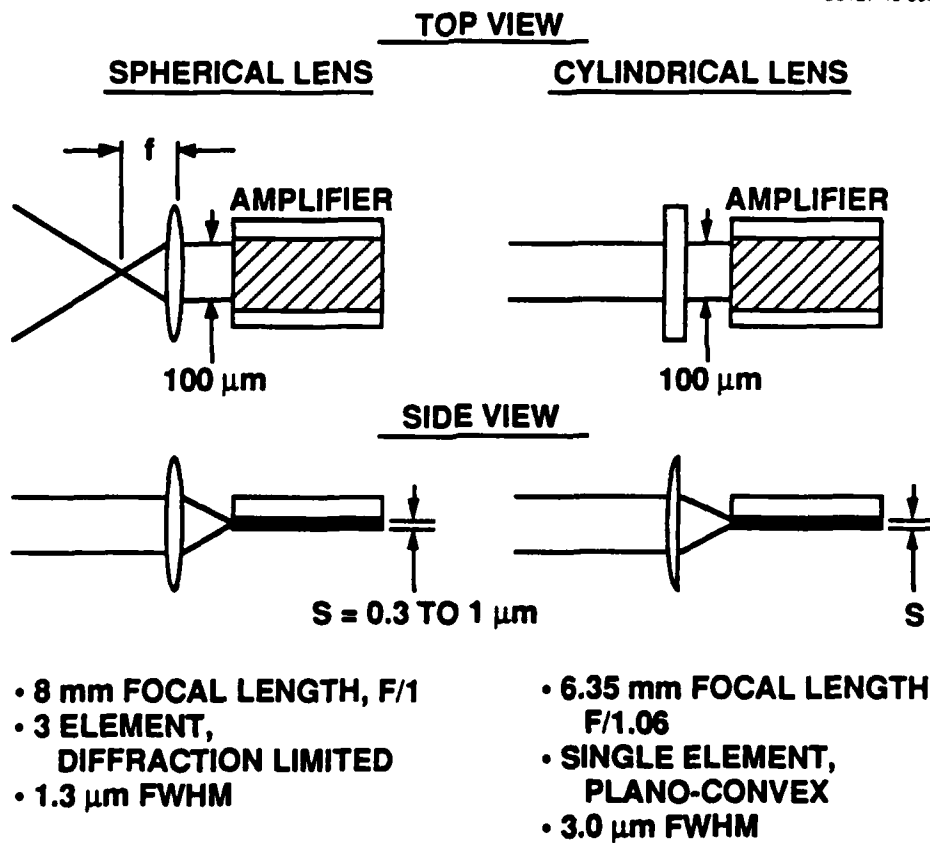


Figure 27. Coupling MO beam into amplifier.

### 4.2.2 MOPA System Equations

Coupling efficiency and small signal gain can be determined from a series of power and optical loss measurements made on the amplifier and on the MOPA system. Refer to Figure 26 for the following discussion. The basic MOPA system powers measured are the input power from the MO,  $P_{MO}$ , observed after attenuation and polarization rotation, and the MOPA output power at the power meter,  $P_D$ . MO power at the amplifier input facet (before coupling in) is define as  $P_F$ , and MOPA output at the facet (outside the amplifier) is defined as  $P_{OUT}$ . Transmission of the optics between the  $P_{MO}$  and  $P_F$  locations is defined as  $T_L$ , and transmission between the  $P_{OUT}$  and  $P_D$  locations is  $T_{OUT}$ .

The small-signal single-pass gain is

$$G_S = \exp((g_0 - \alpha)L) \quad (12)$$

where  $g_0$  is the small-signal gain coefficient,  $\alpha$  is the distributed absorption coefficient, and  $L$  is the amplifier length. With the above definitions in mind the MOPA output can be written as

$$P_{OUT} = P_F \eta_C R_2 G_S^2 \quad (13)$$

where  $\eta_C$  is the coupling efficiency. Since  $P_{OUT} = P_D / T_{OUT}$  and  $P_F = T_L P_{MO}$ , we have

$$\eta_C = (P_D / P_{MO}) / (G_S^2 R_2 T_L T_{OUT}) \quad (14)$$

All quantities on the right side of Eq. (14) are known or are measured during the course of the experiment except for  $G_S$ .

$G_S$  is a variable with respect to amplifier drive current while the coupling coefficient  $\eta_C$  is a constant as long as the optical alignment is fixed. In order to determine the coupling coefficient we need to know at least one data point for the gain. This is accomplished by running the amplifier prior to AR coating as a laser and determining its threshold current value  $I_{th}$ . At laser threshold

$$G_S(\text{threshold}) = (R_1 R_2)^{-1/2} \quad (15)$$

so that if the amplifier as configured in Figure 26 is run at  $I_{th}$ , the coupling efficiency will be given by Eq. (14) with  $G_S = G_S(\text{threshold})$ . Prior to AR coating  $R_1 = 0.32$  and the HR facet

typically has  $R_2 = 0.95$ . Thus under the conditions of the present experiment,  $G_S(\text{threshold}) = 1.814$ .

Once  $\eta_C$  is known, the gain is determined at other values of amplifier drive current from Eq. (14) solved for  $G_S$

$$G_S = ((P_D/P_{MO})/(\eta_C R_2 T_L T_{OUT}))^{1/2} \quad (16)$$

Putting this value of  $G_S$  into Eq. (12) allows us to solve for the gain-length product

$$(g_0 - \alpha)L = \ln(G_S) \quad (17)$$

The presence of the natural log in Eq. (17) is the reason the logarithmic amplifier is required in the MOPA measurement apparatus.

#### 4.2.3 Facet Reflectivity and Coupling Efficiency

Reflectivity of the AR coated facet and coupling efficiency of the MO beam into the amplifier are determined from a single data run. An example of the data is shown in Figure 28 where a plot is made of  $P_D/P_{MO}$  as a function of amplifier heat sink temperature. The amplifier is run at  $I_{th}$ , and the temperature is varied several degrees around the temperature where  $I_{th}$  was measured, in this case  $14^\circ$ . Varying the temperature causes both the refractive index ( $n$ ) and the amplifier length ( $L$ ) to change, thereby changing the single pass phase shift. This causes the Fabry-Perot resonances to shift across the fixed MO wavelength, thereby giving oscillations in the MOPA output.

Facet reflectivity is determined by inserting values of  $\rho_R$  derived from the data of Figure 28 into the  $\rho_R$  equation shown in Figure 25. Local values of  $I_{MAX}/I_{MIN} = \rho_R$  are determined by drawing dashed lines through the peaks and valleys of the oscillatory experimental data. Values of  $P_D/P_{MO}$  and the envelope curves increase at lower temperatures because the small-signal gain increases as the temperature is lowered. Where the envelope lines intersect the solid vertical line at  $14^\circ$  yield  $\rho_R$  at  $G_S(\text{threshold})$ . Since the  $\rho_R$  equation cannot be solved analytically for  $R_1$ , we adjust  $R_1$  by computer until the equation balances. This value of  $R_1$  is then the reflectivity of the AR coated facet.

The facet reflectivity for the amplifier data shown in Figure 28 is  $6.2 \times 10^{-4}$ . This is the best reflectivity measured for the roughly 10 samples that we have studied using this MOPA method. More typical AR coatings exhibited reflectivities in the neighborhood of  $2 \times 10^{-3}$ . Maximum



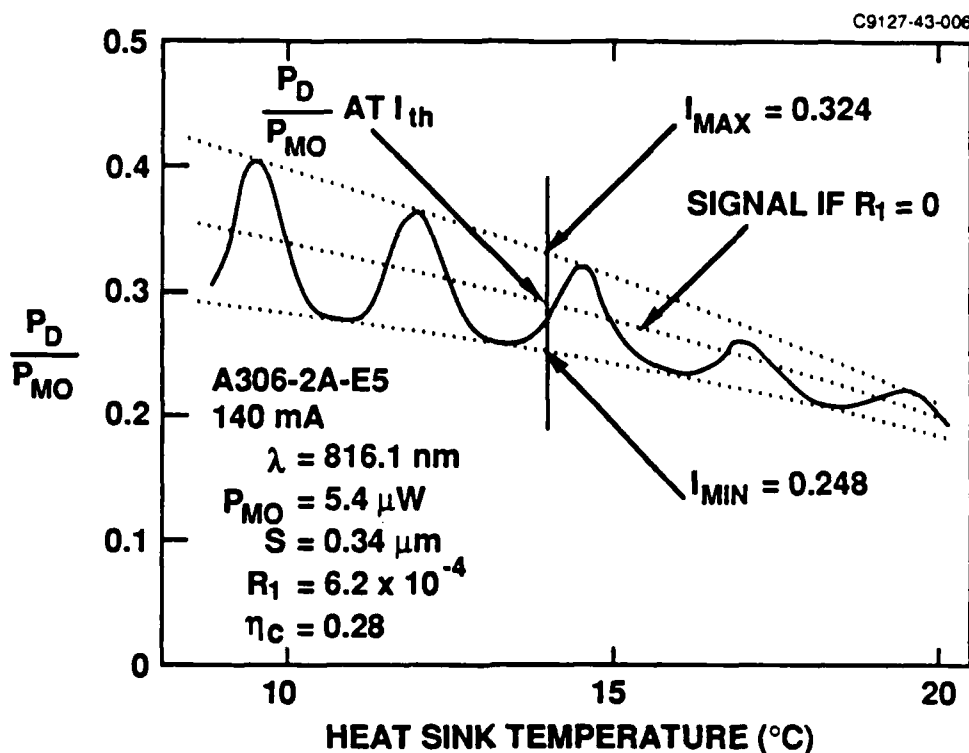


Figure 28. Facet reflectivity and coupling efficiency measurement.

achievable values of  $(g_0 - \alpha)L$  therefore would be limited by the AR coatings to 3.1 (typical) and to 3.7 (best) in the devices studied thus far.

Coupling efficiency is determined by inserting a value for  $P_D/P_{MO}$  derived from Figure 28 at  $I_{th}$  into Eq. (14). This equation assumes that  $R_1 = 0$ , i.e., that there are no multiple reflections. The location of the  $R_1 = 0$  curve for  $P_D/P_{MO}$  is determined by solving the  $G_R$  equation in Figure 25 for  $G_R(\max)$  when  $\delta/2 = \pi$  and for  $G_R(\min)$  when  $\delta/2 = \pi/2$  using the now known values of  $R_1$ ,  $R_2$ , and  $G_S$ . The  $R_1 = 0$  value for  $P_D/P_{MO}$  will be located in the same relative position to the experimental envelope curves as  $R_2 G_S^2$  is relative to  $G_R(\max)$  and  $G_R(\min)$ . For low AR facet reflectivities, this is midway between the envelope curves as shown in Figure 28. For higher reflectivities, the resonance profiles become nonsinusoidal and the  $P_D/P_{MO}$  location is closer to the lower envelope curve.

Coupling efficiency data for seven amplifiers as a function of effective waveguide mode size are shown in Figure 29. Differences in mode sizes were produced by variations in the index of refraction and thickness of the cladding layers encountered on the various growth runs. The 1.0- $\mu\text{m}$  mode was produced by a large optical cavity structure, whereas the other data points are for conventional geometries.

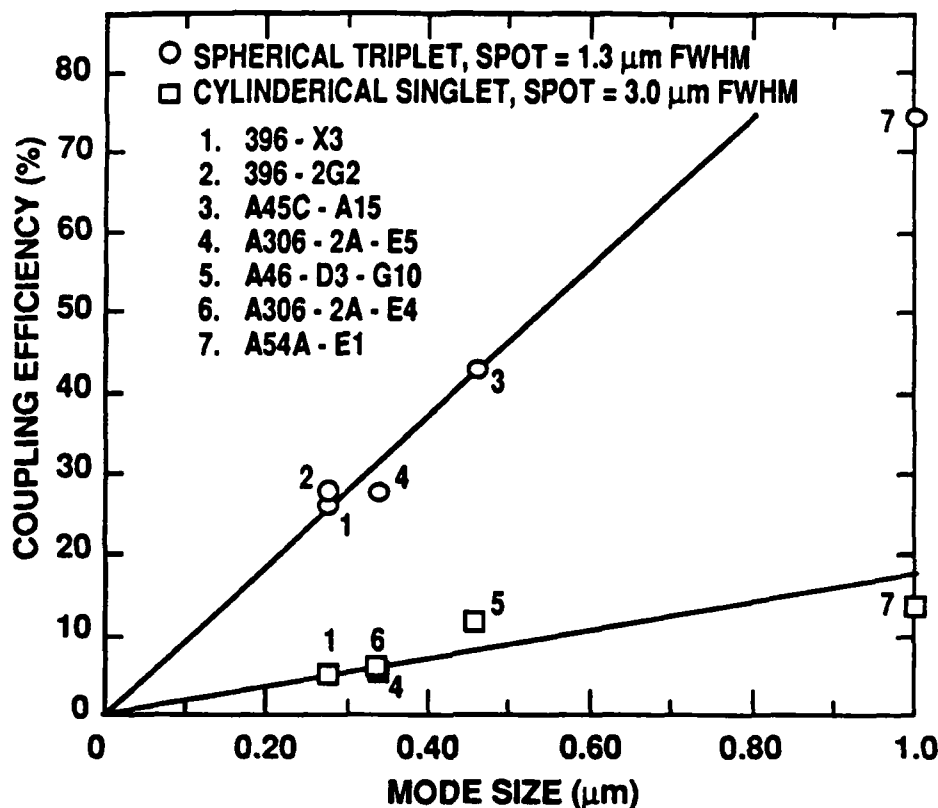


Figure 29. Coupling efficiency results.

Mode size was determined by comparing the measured far-field angular divergence of lasing devices to theoretical curves of divergence versus mode size. The divergences were measured perpendicular to the diode junction plane, and the lasers were from the same growth runs as the amplifiers on which the coupling efficiency measurements were made. Figure 4.13 of Reference 11 and the accompanying definition of effective mode size ( $S$ ) were employed for the theoretical comparisons. We assumed a double exponential near-field waveform for comparisons to Figure 4.13 of Reference 11.

Data are shown in Figure 29 for the two final focusing lenses shown previously in Figure 27. These are fairly typical of lenses that would be employed in practical PC MOPA systems. The spherical lens gives nearly diffraction-limited performance (1.3- $\mu\text{m}$  FWHM spot) and is appropriate for use with single amplifiers which are less than approximately 300  $\mu\text{m}$  wide. Increases in field-curvature will degrade coupling efficiency in wider amplifiers.

The cylindrical lens is a simple singlet and thus does not give diffraction-limited performance (only 3.0  $\mu\text{m}$  spot). However, due to its one dimensional focusing properties it can

be used to feed very wide amplifiers or arrays of amplifiers. Diffraction-limited performance can be produced by multi-element cylindrical lenses, but these were too expensive to purchase for this study. Presumably these would provide spot sizes and coupling efficiencies comparable to the spherical lens investigated here.

The data of Figure 29 show that coupling efficiency for a fixed input spot varies approximately linearly with effective mode size. The coupling also is roughly inversely proportional to input spot size for a fixed mode size. Both of these results are expected since the coupling efficiency is proportional to the overlap integral of the input intensity profile with the amplifier waveguide mode.

What is more interesting is the high values achievable with diffraction-limited optics. A coupling of 43% was observed for a conventional structure mode of  $0.46\text{ }\mu\text{m}$ , and over 70% was seen for a LOC mode of  $1.0\text{ }\mu\text{m}$ . PC MOPA modeling studies indicate that coupling efficiencies of this magnitude should produce good output power and efficiency. Large optical cavity structures are better, but the high numbers exhibited above for conventional structures indicate that the extra effort required to implement the large optical cavity may not be needed.

#### 4.2.4 Gain and MOPA Output Power

The small signal gain-length product was measured for approximately 10 amplifiers as a function of amplifier drive current. Prior to the actual gain measurements we measured MOPA output power ( $P_D$ ) as a function of MO input ( $P_{MO}$ ), and found that  $P_D/P_{MO}$  was flat up to  $P_{MO}$  values of about  $10^{-4}\text{ W}$  and then fell off at a rate of about 3 dB per decade thereafter. To make absolutely sure we were in the small signal gain regime, we always employed  $P_{MO}$  powers in the neighborhood  $5 \times 10^{-6}\text{ W}$ , about a factor of 20 below  $P_{MO}$  values that just started to give gain saturation. This typically gave coupled input powers of less than  $1\text{ }\mu\text{W}$ .

Figure 30 shows a  $(g_0 - \alpha)L$  plot for TE polarization obtained with the apparatus of Figure 26. This amplifier had an AR coated facet reflectivity of  $2 \times 10^{-3}$ , a coupling efficiency of 43%, and an effective mode size of  $0.46\text{ }\mu\text{m}$ . The MO power coupled into the amplifier was about  $0.5\text{ }\mu\text{W}$ . The gain-length product gradually increases from 1 at about 150 mA to a maximum value (if one averages out the resonances) of about 2.8 above currents of about 600 mA. The profile generally resembles the ASE saturated computer simulation in Figure 24. The lack of laser oscillations at the highest currents may indicate that part of the gain saturation is caused by thermal effects. At 1 A of drive current, the  $100 \times 500\text{-}\mu\text{m}$  amplifier is successfully surviving a CW current density of  $2000\text{ Amps/cm}^2$ . The high current density and the minimal optical power extraction during gain measurements both contribute to high junction temperatures.

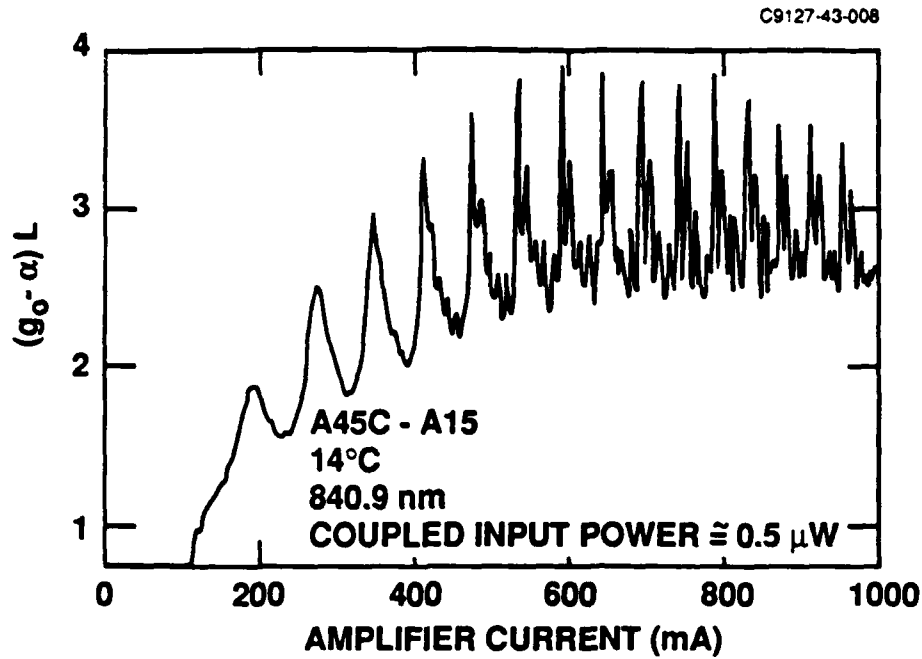


Figure 30. TE gain-length product.

Fabry-Perot resonances are clearly evident in Figure 30. As explained in Section 4.1.2., since the refractive index and the amplifier length are functions of current and temperature, changing the drive current will affect the single pass phase shift ( $\delta/2$  in Figure 25) thereby causing resonances in the MOPA output. For currents less than 300 mA (low gain) the resonances are roughly sinusoidal, but become very sharp at currents above 500 mA. We believe the multiple spikes seen in each cycle at high currents are multiple resonances caused by the generation of higher order transverse modes. The appearance of the multiple spikes correlates with the deterioration of MOPA output beam quality.

The gain-length product for TM polarization is shown in Figure 31 for run conditions similar to those of the TE case. We have assumed that the coupling efficiency is the same as for the TE case in order to derive the y-axis calibration. The value of  $(g_o - \alpha)L$  gradually increases to a maximum value of about 1.7 at about 600 mA and thereafter remains constant, in a manner similar to the TE case. Due to the lower gains, Fabry-Perot resonances are relatively weak. The large negative-going oscillations are due to noise.

From the above TE and TM gain-length product data we find that the maximum gain coefficients are  $g_{TM} = 29 \text{ cm}^{-1}$  and  $g_{TE} = 51 \text{ cm}^{-1}$  for  $L = 500 \text{ }\mu\text{m}$  and assuming  $\alpha = 5 \text{ cm}^{-1}$ . The ratio of TM to TE gain coefficient at high current is  $29/51 = 0.57$ . PC MOPA modeling studies indicate that performance improves as this ratio increases since the overall system gain is

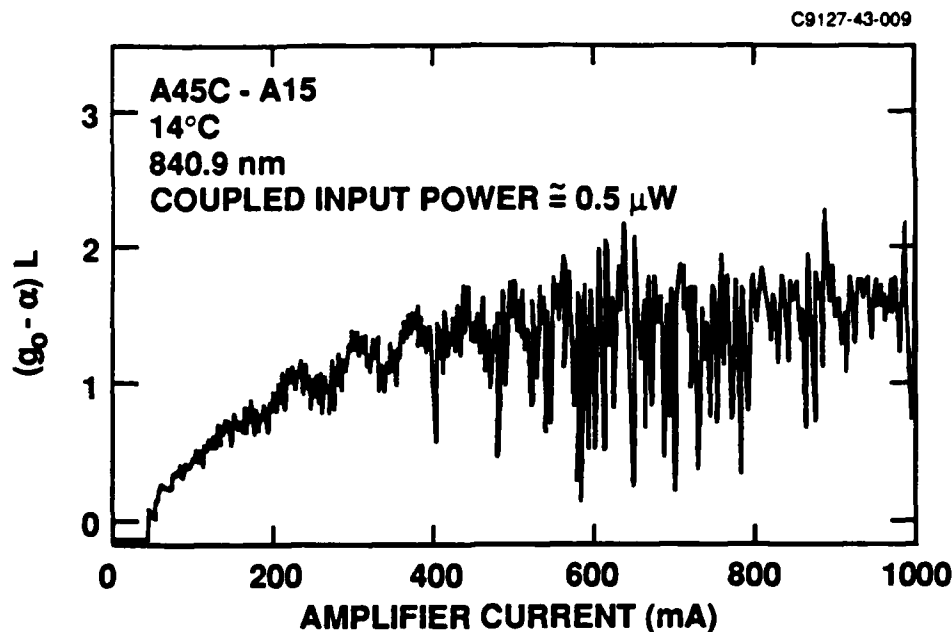


Figure 31. TM gain-length product.

larger. Values of 0.8 or above would be more desirable, but ratios in the range seen here are acceptable. A fairly low ratio is to be expected due to the polarization selection of the quantum well structure (see Reference 9).

The effect of increasing the input power to the amplifier by about a factor of 1000 is shown in Figure 32. Here the MO attenuator is adjusted for maximum transmission, giving about 0.6 mW coupled into the amplifier. The log amp has been removed to provide a linear output power versus amplifier drive current plot. The output is still synchronously detected as before so that no spontaneous emission appears on this plot.

With 0.6 mW input, the TE MOPA output ( $P_{OUT}$ ) varies approximately linearly with drive current to values of about 110 mW at 1000 mA. This is over 22 dB of large signal gain which shows no evidence of rolling over. The effective gain-length product ( $0.5 \ln(110/0.6)$ ) seen here is 2.6, which is only slightly below the small signal value of 2.8. For TM polarization power output is also linear with drive current and yields a maximum output of 15 mW at 1000 mA. The effective gain-length product in this case is 1.6 which also shows minimal saturation compared to the small signal value of 1.7. Fabry-Perot resonances in the MOPA output are clearly seen for both polarizations in Figure 32.

We have employed our computer model to simulate this experiment using the amplifier parameters measured in this study. For the experimental conditions of Figure 32, the model

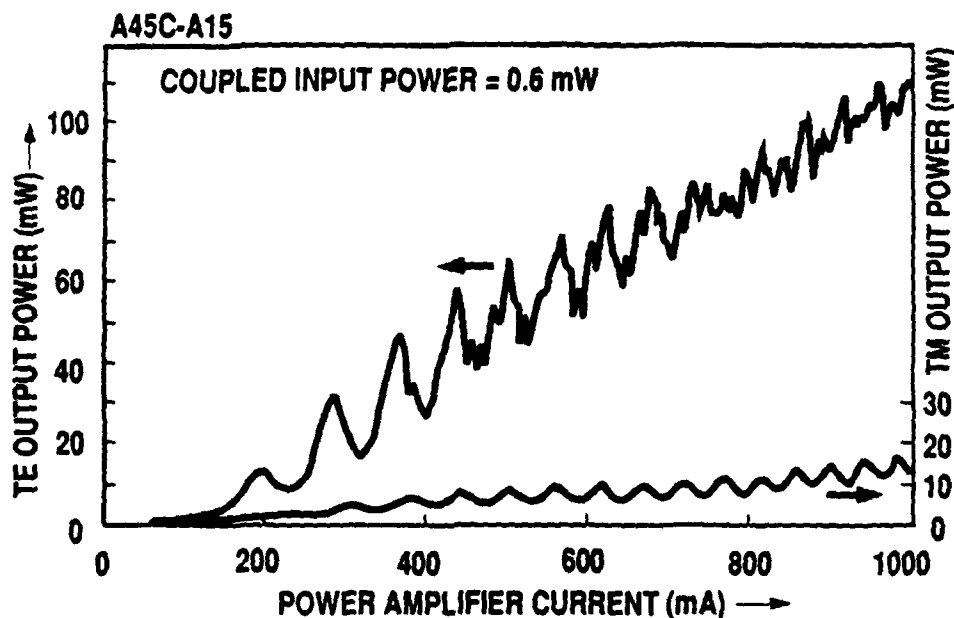


Figure 32. Two-pass MOPA output power.

predicts that the two-pass TE MOPA should have an output of 125 mW at 1000 mA, and 68 mW at 500 mA. Observed values are about 110 mW and 55 mW, indicating the modeling is accurate to within 15 to 25%.

Extending the model to higher MO inputs shows that the MOPA output of Figure 32 is limited by MO power rather than by gain. If the coupled input could be increased to 20 mW, the two-pass MOPA output is predicted to be 510 mW at 1000 mA and 240 mW at 500 mA. If operated as a laser (optimized facet coatings), the model predicts that this device would have an output of 1.1 W at 1000 mA and 420 mW at 500 mA. The experimentally coupled input of 0.6 mW thus extracted only 10% and 13% of the available inversion at 1000 mA and 500 mA, respectively. If the coupled input could be increased to 20 mW, the extraction efficiencies would increase to 46% and 57%.

A properly operating PC MOPA has about 90% of the power extracted on the final two passes, so that the four-pass PC MOPA typically has the output power of a well saturated two-pass conventional MOPA. Use of a device such as that shown in Figure 32 in an optimized PC MOPA thus is expected to give diffraction-limited output powers of about 250 to 500 mW. This corresponds to output power densities of 500 to 1000 W/cm<sup>2</sup> of diode junction area. The

electrical to optical conversion efficiency of the PC MOPA would be about half that of an optimized laser of the same design.

#### 4.2.5 MOPA Output Beam Quality

A perfect phase conjugate mirror will correct any phase aberrations encountered on the first two passes of the amplifier when the phase conjugated beam makes the second set of passes. However, if the phase conjugate mirror system is not operating properly, some degradation in the output beam quality of the PC MOPA will result. Two possible failure mechanisms exist which are related to the level of aberrations generated by the amplifiers. First, if the aberrations are too large, the phase conjugator may not be able to handle them. Second, if the distortions are too large, the optical system leading from the amplifier to the conjugator may not transmit the entire output beam without clipping. Any such aperturing effect will result in a loss of phase distortion information which will go uncorrected.

Previous experience has shown that the major limitation with BaTiO<sub>3</sub> systems is not the conjugator, but is the aberration handling capabilities of the optical system. For amplifiers of the size employed in this study, we have found that optical systems are reasonably easy to design which can handle beams with angular divergences up to about six times the diffraction-limit. Thus, AlGaAs amplifiers will be usable in practical PC MOPA systems if the two-pass far-field output beam divergence is less than about six times the diffraction limit. If beam divergences larger than this are generated, either more complex optics will be needed or some type of transverse mode control on the amplifier will have to be included.

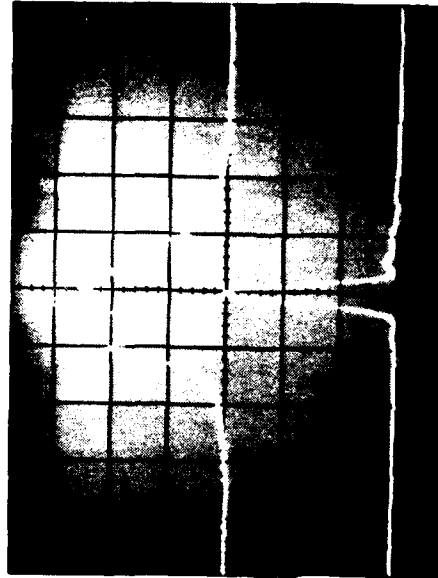
Near- and far-field output profiles after two passes of the amplifier are shown in Figure 33. The device is the same one shown in Figure 32, and is operated under the same conditions. The numbers in the format X,Y below each far field label in Figure 33 are the far field divergences compared to the diffraction limit. X uses full width at half maximum (FWHM) as the measurement reference, and Y employs full width at  $e^{-2}$  (FWe<sup>-2</sup>) power points as the criterion. All measurements assume a Gaussian relationship in the near-field to far-field transformation.

At the left of Figure 33 are shown the near- and far-field intensity distributions produced by the master oscillator input beam at the amplifier facet. The MO near-field (image of the beam on the amplifier facet) is a 100- $\mu\text{m}$ -FWe<sup>-2</sup> wide Gaussian beam. The corresponding far-field is also Gaussian with a divergence of approximately 0.62° FWe<sup>-2</sup> which is diffraction-limited at the operating wavelength of 841 nm employed here.

Two-pass MOPA profiles at 150- and 390-mA drive currents are shown at the right of Figure 33. Even at the relatively low currents shown here double passing the amplifier introduces some phase aberrations and intensity fluctuations. The near-field profiles fluctuate

C9127-43-010

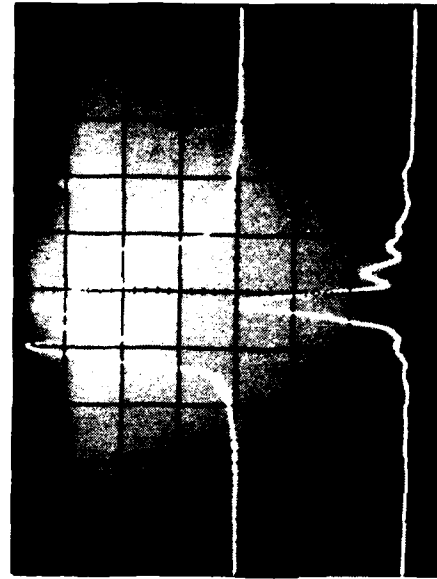
MOPA OUTPUT



150 mA

NEAR FIELD

FAR FIELD  
1.4, 1.3

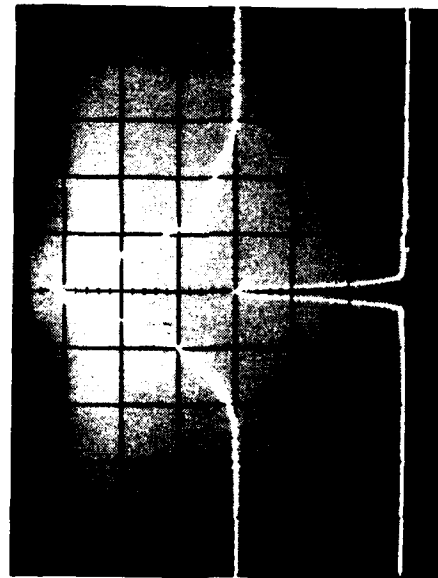


390 mA

NEAR FIELD

FAR FIELD  
1.7, 2.5

MASTER OSCILLATOR



NEAR FIELD

FAR FIELD  
1, 1

X, Y = FWHM,  $\text{FWHM}^2$  FAR FIELD DIVERGENCE  
COMPARED TO THE DIFFRACTION LIMIT

Figure 33. Near-field and far-field profiles at low drive currents.



rapidly compared to the input beam, and the far-field profiles degrade slowly as the current is raised, reaching a divergence of about twice the diffraction-limit at 390 mA. The relatively good far-field quality of these examples would indicate that the phase across the output aperture is still relatively uniform even though the near-field intensity departs substantially from the uniform Gaussian used as the input.

Profiles for higher amplifier currents are shown in Figure 34. At 500 mA the near-field has degenerated into a series of well-defined spikes which indicates that several higher-order transverse modes contain most of the output power. The corresponding far-field has a dominant lobe which is about 2.5 times diffraction limited, but additional sidelobes extend out to angles that are about eight times the diffraction limit. Operating at this drive current in a PC MOPA with typical phase conjugator optics would result in some loss of information, and a small degradation in the output beam quality.

At 1000 mA, the near-field pattern shows rapid fluctuations, indicating that power is shared among many high-order transverse modes. The far-field has completely degenerated with a divergence of somewhere between 13 and 40 times the diffraction limit. It would be difficult to use this device at 1000 mA drive levels without encountering serious information loss in the phase conjugator optics and a resultant serious degradation in the PC MOPA output beam quality.

#### 4.3 DETERMINATION OF $I_{SAT}$ FROM LASER P-I CURVES

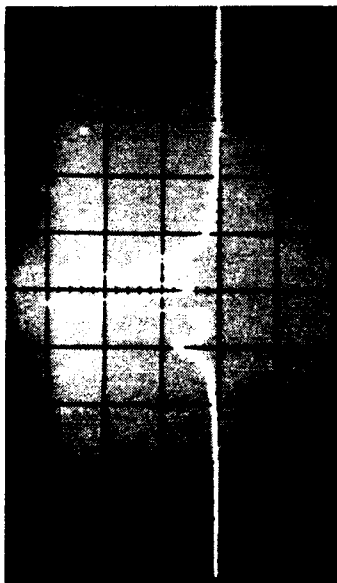
The last important amplifier characteristic to be measured is the saturation parameter,  $I_{SAT}$ . It could be deduced from MOPA measurements using the apparatus of Figure 26 if a master oscillator with an output large enough to significantly saturate the gain were employed. The 15 mW MO used in this study was marginal at best, so we employ a method which uses the light generated by the amplifier operated as a laser to perform the gain saturation. Determination of  $I_{SAT}$  is accomplished by comparing the model results to experimental power versus current (P-I) curves.

During the coating procedures P-I curves are measured for all the amplifiers. A pair of curves are shown in Figure 35 for the same amplifier described in the previous section. The right hand curve labeled 0.32/0.32 ( $R_1/R_2$ ) was obtained before any coatings were applied and thus has  $R_1 = 0.32$  and  $R_2 = 0.32$  (reflectivity of uncoated AlGaAs). The left-hand curve labeled 0.32/0.95 was obtained after the high R coating was applied to the back facet and prior to AR coating the front facet. It therefore still has  $R_1 = 0.32$  but now  $R_2 = 0.95$ .

The laser threshold of the 0.32/0.32 curve is at  $I_{th} = 150$  mA corresponding to a gain of  $G_S = G_{th} = (R_1 R_2)^{-1/2}$ . Assuming that the amplifier did not change characteristics during the

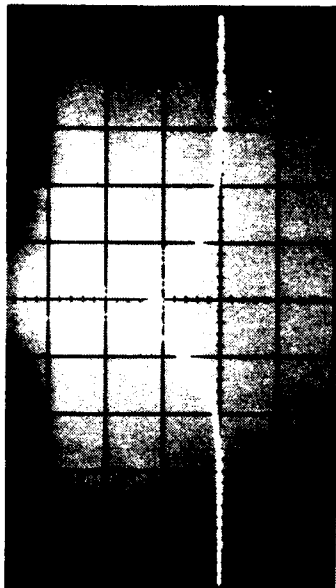
C9127-43-011

500 mA



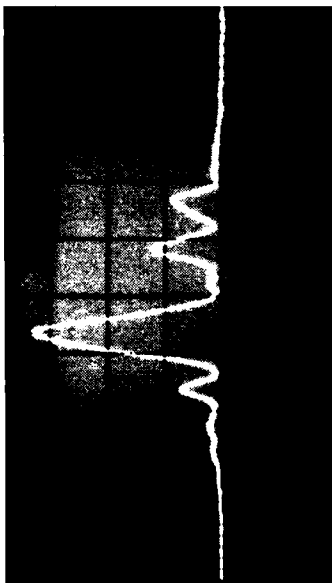
NEAR FIELD

1000 mA

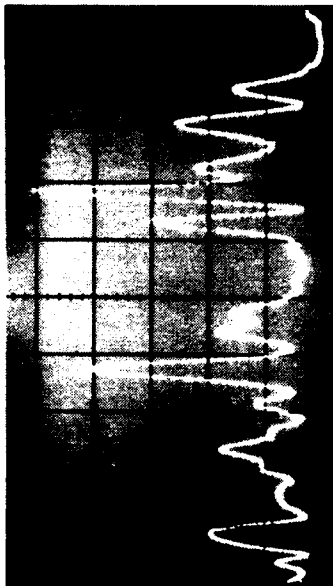


NEAR FIELD

FAR FIELD  
2.5, 7.9



FAR FIELD  
13, > 40



X, Y = FWHM,  $\text{FWHM}^{-2}$  FAR FIELD DIVERGENCE COMPARED TO THE DIFFRACTION LIMIT

Figure 34. Near-field and far-field profiles at high drive currents.

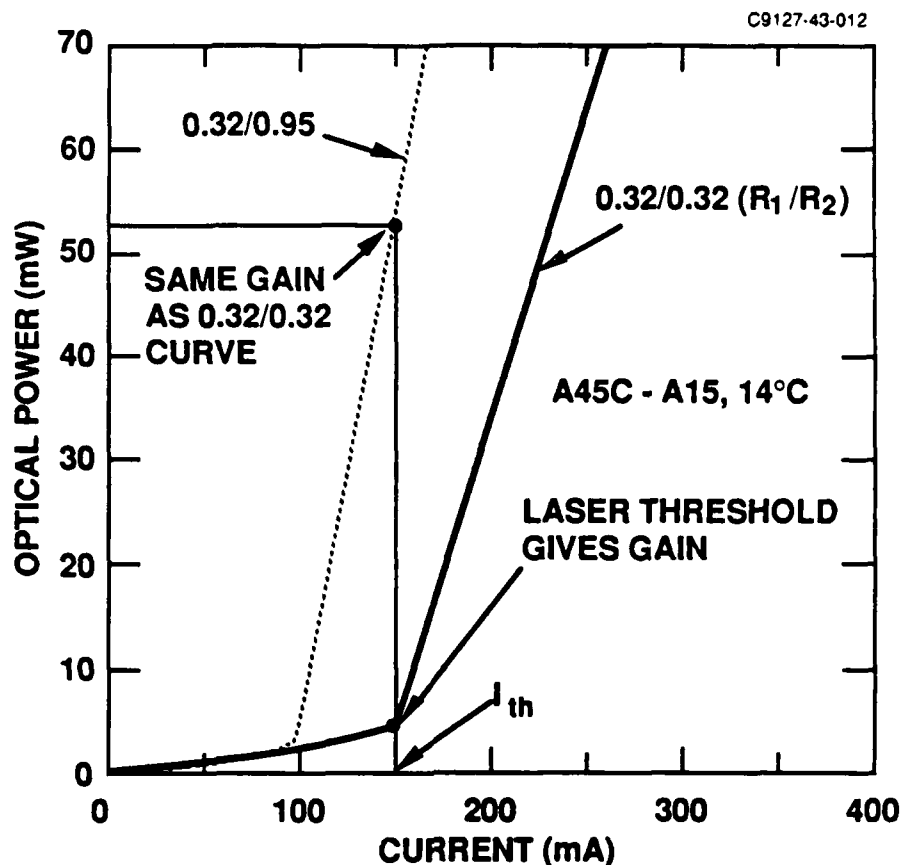


Figure 35. P-I curves used to determine  $I_{SAT}$ .

back facet ( $R_2$ ) coating, the gain at 150 mA for the 0.32/0.95 curve will also be  $G_{th}$  only now the device is far above threshold and has an output of 53 mW. All input parameters required to model the 0.32/0.95 curve at 150 mA are now known from Figure 35 or from the preceding measurements except for  $I_{SAT}$ .  $I_{SAT}$  can therefore be determined by varying  $I_{SAT}$  in the model until the calculated output agrees with the actual output of 53 mW.

Saturation parameters determined in this way fell in the range of 200 kW/cm<sup>2</sup> to 300 kW/cm<sup>2</sup> which are typical for AlGaAs lasers.  $I_{SAT}$  for the device in Figure 35 was 300 kW/cm<sup>2</sup>. PC MOPA modeling studies indicate that  $I_{SAT}$  values in this range are consistent with high output power and good electrical-to-optical conversion efficiency.

#### 4.4 SUMMARY OF AMPLIFIER PARAMETERS

A number of parameters important for PC MOPA applications were measured for large area amplifiers grown and fabricated at HRL. The devices studied were SQW GRIN-SCH

structures with effective waveguide mode dimensions in the range of 0.28 to 1.0  $\mu\text{m}$ . The amplifiers were 100  $\mu\text{m}$  wide and 500  $\mu\text{m}$  long. Most measurements were made with a two-pass, single-ended MOPA apparatus where the MO entered and exited through one amplifier facet and the other facet was high-reflectivity coated.  $I_{\text{SAT}}$  was determined by comparisons of computer simulations with P-I curves for the amplifiers operated as lasers.

A summary of the measured amplifier parameters is shown in Table 1 along with desired target values required for excellent PC MOPA performance. Gain-length products in the range 2.5 to 3.0 were observed, which were somewhat lower than the desired value of four. A contributing factor to the nonoptimal gain values were the AR facet coatings which were measured to be in the range  $6 \times 10^{-4}$  (best measured) to  $2 \times 10^{-3}$  (typical) using the MOPA method. However, in several cases the observed gain "saturation" may have been caused by heating of the diode junction at the high (2000 Amps/ $\text{cm}^2$ ) drive current densities encountered. Additional work on AR coatings and even better methods of diode bonding is needed.

The high reflectivity coating values of 0.95 or greater typically produced by our six layer  $\text{Al}_2\text{O}_3/\text{Si}$  process leaves little room for improvement. The observed coupling efficiencies of up to  $\eta_C = 0.7$  for diffraction-limited optics and a large optical cavity waveguide also are about as good as can be hoped for. Similarly, the measured saturation parameters of 200 to 300  $\text{kW}/\text{cm}^2$  are in the typical range for AlGaAs lasers and thus meet our target goal.

The tolerable amount of beam aberrations after two passes of the amplifier is dependent primarily upon the phase conjugator optical system. Present conventional approaches to optical design can tolerate beams that diverge by six times the diffraction limit. Measured beam quality figures for our amplifiers ranged from 1 to >10 times the diffraction limit. However, the beam quality was highly current dependent and the highest gains were attained before the beam degraded to the 6X diffraction limit level. The amplifiers are thus compatible with present phase conjugator optical system designs.

Items 3 through 6 in Table 1 equal or are very close to the goals set in this program. Items 1 and 2 are close to the goals but require additional work. Even though the amplifier characteristics are not quite as good as possibly might be attained, a PC MOPA employing amplifiers with the characteristics observed in Table 1 would perform well.

TABLE 1. AlGaAs Power Amplifier Characteristics.

C9127-43-013

PARAMETER	OBSERVED	GOAL
1. SMALL SIGNAL GAIN LENGTH PRODUCT ( $g_0 - \alpha$ )L	2.5 TO 3.0	4.0
2. AR FACET REFLECTIVITY ( $R_1$ )	$6 \times 10^{-4}$ (BEST) $2 \times 10^{-3}$ (TYPICAL)	$10^{-4}$
3. HR FACET REFLECTIVITY ( $R_2$ )	$\geq 0.95$	1.0
4. COUPLING EFFICIENCY ( $\eta_c$ )	0.05 TO 0.7 STRUCTURE AND OPTICS DEPENDENT	HIGH, 50% IS GOOD
5. SATURATION PARAMETER ( $I_{SAT}$ )	200 TO 300 kW/cm <sup>2</sup>	HIGH, 200 TO 300 kW/cm <sup>2</sup> TYPICAL FOR AlGaAs LASERS
6. BEAM QUALITY	1 TO > 10X THE DIFFRACTION LIMIT, CURRENT DEPENDENT; HIGHEST GAINS ATTAINED AT < 6X	< OPTICAL SYSTEM LIMITS, TYPICALLY 6X THE DIFFRACTION LIMIT

## REFERENCES

1. W.T. Tsang, Appl. Phys. Lett. 39, 134 (1981).
2. W.T. Tsang, IEEE J. Quantum Electron. QE-20, 1119 (1984).
3. L.J. Van Ruyven, J. Lumin 29, 123 (1984).
4. R.D. Burnham, W. Streifer and T.L. Paoli, J. Cryst. Growth 68, 370 (1984).
5. N. Holonyak, Jr., R.M. Kolbas, R.D. Dupius, IEEE J. Quantum Electron. QE-16, 170 (1980).
6. B. deCremoux, in Proceedings of the European Solid State Device Research Conference (ESSDERC) 1985, Solid State Devices 85, edited by P. Balk and O.G. Folberth (Elsevier, Amsterdam, 1986), p. 83.
7. W.T. Tsang, in "Semiconductors and Semimetals," edited by R.K. Illardson and A.C. Beer (Academic, New York, 1985), Vol. 22A, p. 95.
8. J. Nagle, S. Hersee, M. Krakowski, T. Weil and C. Weisbuch, Appl. Phys. Lett. 49, 1325 (1986).
9. Masamichi Yamanishi and Ikuo Suemune, Japan. J. Appl. Phys. 23, L35 (1984).
10. G. Eisenstein, AT&T Bell Labs. Tech. J. 63, 357 (1984).
11. G.H.B. Thompson, "Physics of Semiconductor Laser Devices" (John Wiley & Sons, Chichester, 1985), pp. 181-196.
12. J.N. Schulman, Mat. Res. Soc. Symp. Proc. 56, 279 (1986).
13. William. J. Fritz, IEEE J. of Quantum Electron. 26, 68 (1990).
14. Technical assistance from Jeff Mott of HDOS dramatically reduced the development time for In fluxless soldering.
15. J. Thomas Cox and Georg Hass, "Antireflection Coatings for Optical and Infrared Materials", in Physics of Thin Films 2, edited by Georg Hass and Rudolf E. Thun (Academic Press, London, 1964), p. 239.
16. Reference 11, pp. 117-118.
17. Basil W. Hakki and Thomas L. Paoli, J. Appl. Phys. 44, 4113 (1973).
18. Reference 11, pp. 82 and 83.
19. T. Mukai and Y. Yamamoto, IEEE J. Quantum Electron, Vol QE-16, 1028-1034, June 1981.